Optical excitations in organic molecules, clusters, and defects studied by first-principles Green's function methods

Murilo L. Tiago[1] and James R. Chelikowsky[1,2]

[1]*Center for Computational Materials, Institute for Computational Engineering and Sciences,*
University of Texas, Austin, Texas 78712, USA
[2]*Departments of Physics and Chemical Engineering, University of Texas, Austin, Texas 78712, USA*

Spectroscopic and optical properties of nanosystems and point defects are discussed within the framework of Green's function methods. We use an approach based on evaluating the self-energy in the so-called GW approximation and solving the Bethe-Salpeter equation in the space of single-particle transitions. Plasmon-pole models or numerical energy integration, which have been used in most of the previous GW calculations, are not used. Fourier transforms of the dielectric function are also avoided. This approach is applied to benzene, naphthalene, passivated silicon clusters (containing more than one hundred atoms), and the F center in LiCl. In the latter, excitonic effects and the $1s \rightarrow 2p$ defect line are identified in the energy-resolved dielectric function. We also compare optical spectra obtained by solving the Bethe-Salpeter equation and by using time-dependent density-functional theory in the local, adiabatic approximation. From this comparison, we conclude that both methods give similar predictions for optical excitations in benzene and naphthalene, but they differ in the spectra of small silicon clusters. As cluster size increases, both methods predict very low cross section for photoabsorption in the optical and near ultraviolet ranges. For the larger clusters, the computed cross section shows a slow increase as a function of photon frequency. Ionization potentials and electron affinities of molecules and clusters are also calculated.

PACS number(s): 71.15.Qe, 73.21.La, 73.22.Lp, 78.67.−n

I. INTRODUCTION

Universality and predictive power are characteristic features of good first-principles theories. Such theories are invaluable as guides for experimental work, especially when knowledge about the system being investigated is limited. Density-functional theory (DFT) is recognized as state-of-the-art theory for the calculation of various ground-state properties of electronic systems from first principles, having been applied to a variety of different systems ranging from crystalline semiconductors to surfaces and nanostructures.[1] In contrast, DFT has known difficulties in predicting quantities associated with excited states, which is not surprising since it was first proposed as a ground-state theory. As an example, the electronic band structure provided by DFT consistently shows an underestimated gap between valence and conduction bands.[1–4] As a consequence, the electronic band structure provided by DFT gives poor predictions for the onset of photoemission and inverse photoemission.[2,4] Exact-exchange functionals improve results considerably for molecular systems,[5] but more work is needed in crystalline systems.[6] Gap narrowing also affects the linear optical spectrum, when calculated from single-electron transitions from the valence band to the conduction band.[4,7]

Spectroscopic and optical properties of semiconductors have been successfully predicted from *ab initio* Green's function methods.[4,7] The GW approximation has been used to provide the quasiparticle band structure of semiconductors, large-gap insulators, metals, surfaces, nanostructures, and other materials.[4] By solving the Bethe-Salpeter equation for electrons and holes, the linear optical spectrum can also be obtained, providing reliable results for the optical gap and excitonic effects.[7–11] Since knowledge of the electron self-

energy is required in solving the Bethe-Salpeter equation (BSE), this method is often refered to as GW+BSE.[12] Although powerful, the GW+BSE method is very complex when applied to nonperiodic systems, especially when discrete Fourier analysis is not applicable and approximations such as the generalized plasmon pole model[2] do not lead to substantial simplification. Some materials that fall in this category are confined systems: quantum dots, clusters, molecules, and nanostructures. On the other hand, nanostructures are now the subject of intense work due to promising technological applications and recent advances in the preparation of artificial nanostructures.[13,14] At the same time, significant effort has been dedicated on the theory side. Some of the difficulties one may encounter by applying the GW approximation to large molecules were emphasized recently.[15,16] So far, reliable calculations of electronic self-energy within the GW approximation have been done for confined systems with up to a few tens of atoms.[8,9,17–19] Similarly, the Bethe-Salpeter equation has been solved for a limited number of confined systems. During the last decade, optical properties of confined systems have been investigated within time-dependent DFT, often with very good results.[7,20] Time-dependent density DFT in the local, adiabatic approximation (TDLDA) is formally simpler than the GW+BSE theory, but at the same time directed towards solving the same problem: predicting optical properties and neutral excitations in an electronic system. A drawback of TDLDA is that it reportedly fails to predict correct optical gaps and excitonic effects in extended systems.[7,21] Alternative TDDFT functionals which include many-body effects have been proposed.[21–25]

As mathematical simplification, applications of the GW+BSE method in nanostructures frequently impose artificial periodicity by placing the electronic system in a large

supercell.[17] This is a perfectly justifiable procedure, but it has the obvious deficiency of increasing the computational effort when supercells are required to be large. A more efficient procedure would be to take advantage of properties intrinsic to confined systems and design a numerical implementation of such Green's function methods, and we now propose one such implementation. A key ingredient is electronic screening. We incorporate it into the theory by computing the electron polarizability function in two approximations: random-phase approximation (RPA) and TDLDA. The electron self-energy is calculated from first principles and the Bethe-Salpeter equation is set and solved in the space of single-particle transitions. In this framework, many-body functions are expressed as matrices in this transition space and in energy (frequency) representation. Fourier transforms are not needed, and energy integrations are evaluated by integrations over poles. Portions of this work have been reported earlier.[26]

The methodology proposed here is applied to a number of interesting cases. One of them is isolated oligoacenes, for which extensive experimental data is available but the only GW-based analysis known to us have been published recently.[15] The second application is in silicon nanoclusters, studied previously within TDLDA[20] and, for the smaller clusters, GW+BSE.[8,18] Here, we investigate clusters with bulklike crystalline structure and report benchmark GW+BSE calculations for clusters with more than one hundred silicon atoms. The last application is in the F-center defect in LiCl. This is a challenging case, with characteristics of both confined and periodic system. We show that the resulting optical spectrum correctly contains both the signature of defect levels located within the band gap *and* electron-hole interactions. The latter manifest themselves in the energy-resolved dielectric function as an exciton feature below the electronic band gap. TDLDA is shown to predict an optical transition between two defect levels, but the exciton feature is not found. The paper is organized as follows: in Sec. II, we present the theoretical framework, starting from TDLDA and continuing through the GW method and solution of the Bethe-Salpeter equation. Section III is devoted to applications, containing one subsection for each particular system: oligoacenes, silicon clusters, and F center in LiCl. We draw final conclusions in Sec. IV.

II. THEORY

A. Linear response within TDLDA

Gross and Kohn[27] have shown how to extend DFT to the time-dependent case by analyzing the effect on the charge density upon the action of an external potential that changes in time. Their theoretical approach can be further simplified by making use of two assumptions:[7,20,28] adiabatic limit, and local-density approximation, under which the exchange-correlation kernel is instantaneous in time and a sole function of charge density at each point in space. This is the time-dependent local-density approximation (TDLDA).[20,28–30]

When the external potential is due to an applied electric field, the linear response in charge density ρ is related to the

external potential via a response function (the polarizability) according to

$$\Pi_f(1,2) = \frac{\delta\rho(1)}{\delta V_{ext}(2)}, \quad (1)$$

where we use a many-body notation for space-time and spin variables: $(1) = (\mathbf{r}_1, t_1, \tau_1)$. The subscript f indicates that the response function above is calculated within TDLDA. Working in frequency domain,[28] the TDLDA polarizability can be written as a sum over normal modes,

$$\Pi_f(\mathbf{r}, \mathbf{r}'; E) = 2\sum_s \rho_s(\mathbf{r})\rho_s(\mathbf{r}') \left[\frac{1}{E - \omega_s + i0^+} - \frac{1}{E + \omega_s - i0^+} \right], \quad (2)$$

where the normal modes of excitation in the system are denoted by ω_s, and 0^+ represents a positive infinitesimal.[93] We assume $\hbar = 1$ throughout. The factor of 2 comes from summation over spin indices. Still following the frequency-domain formulation by Casida,[20,28] the amplitudes $\rho_s(\mathbf{r})$ are obtained by solving a generalized eigenvalue problem. In order to obtain the desired eigenvalue equation, we first expand ρ_s in a series of single-particle transitions from an occupied level v to an unoccupied level c:

$$\rho_s(\mathbf{r}) = \sum_{vc} X_{vc}^s \varphi_v(\mathbf{r})\varphi_c(\mathbf{r}) \left(\frac{\varepsilon_c - \varepsilon_v}{\omega_s} \right)^{1/2}, \quad (3)$$

where Kohn-Sham eigenvalues are denoted ε_i, with corresponding eigenfunctions φ_i. For clarity, we reserve indices v, v' for occupied orbitals and indices c, c' for unoccupied orbitals. The coefficients X above satisfy an eigenvalue equation in (ω^2) (Ref. 28):

$$\mathbf{R}^{1/2}[\mathbf{R} + 4(\mathbf{K}^x + \mathbf{K}^{LDA})]\mathbf{R}^{1/2}\mathbf{X} = \omega_s^2 \mathbf{X}, \quad (4)$$

where $\mathbf{R}$, $\mathbf{K}^x$, and $\mathbf{K}^{LDA}$ are matrices in the space of single-particle transitions:

$$R_{vcv'c'} = \delta_{vv'}\delta_{cc'}[\varepsilon_c - \varepsilon_v], \quad (5)$$

$$K_{vcv'c'}^x = \int d\mathbf{r} \int d\mathbf{r}' \varphi_v(\mathbf{r})\varphi_c(\mathbf{r})V(\mathbf{r},\mathbf{r}')\varphi_{v'}(\mathbf{r}')\varphi_{c'}(\mathbf{r}'), \quad (6)$$

$$K_{vcv'c'}^{LDA} = \int d\mathbf{r}\varphi_v(\mathbf{r})\varphi_c(\mathbf{r})f_{xc}(\mathbf{r})\varphi_{v'}(\mathbf{r})\varphi_{c'}(\mathbf{r}). \quad (7)$$

The generalized eigenvectors $\mathbf{X}$ are normalized so that $\mathbf{X}^s\mathbf{X}^{s'} = \delta_{ss'}$. Throughout this article, eigenfunctions φ are assumed to be real functions. Indeed, they can be made real if the Kohn-Sham Hamiltonian is real and the electronic system is confined. This assumption is used in Eqs. (2)–(4). A notable situation when the equations above should be modi-

fied is in periodic systems, when eigenfunctions are often expressed as Bloch functions. The generalization to complex eigenfunctions is known.[7,21] Also, we assume that the system has an energy gap and it is spin-unpolarized, although this is not an essential assumption and the same framework holds for gapless systems (e.g., the F center in LiCl, Sec. III C) as well. There are extensions of TDLDA to spin-polarized and/or gapless systems.[20,28,30] Exchange-correlation effects are included in the kernel $f_{xc} = \frac{\delta V_{xc}}{\delta \rho}$, which is a local, energy-independent quantity within TDLDA. The Coulomb potential is simply $V(\mathbf{r}, \mathbf{r}') = \frac{e^2}{|\mathbf{r} - \mathbf{r}'|}$.

Once the eigenvalue problem is solved, one can easily compute the electrostatic polarizability tensor,

$$\alpha_{\beta\gamma} = \frac{e^2}{m} \sum_s \frac{\mathcal{F}_s^{\beta\gamma}}{\omega_s^2}, \tag{8}$$

where m is the electron mass and $\mathcal{F}_s^{\beta\gamma}$ is the oscillator strength along the three Cartesian components $\beta, \gamma = \{x, y, z\}$,

$$\mathcal{F}_s^{\beta\gamma} = 4m\omega_s \left(\int d\mathbf{r} \rho_s(\mathbf{r}) \beta \right) \left(\int d\mathbf{r} \rho_s(\mathbf{r}) \gamma \right). \tag{9}$$

By construction, the TDLDA polarizability satisfies the oscillator-strength sum rule,

$$\sum_s \mathcal{F}_s^{\beta\beta} = (\text{number of valence electrons}). \tag{10}$$

Another quantity of interest is the cross section for absorption of light in a confined system:

$$\sigma(E) = \frac{2\pi^2 e^2}{mc} \sum_s \frac{1}{3} \sum_\beta \mathcal{F}_s^{\beta\beta} \delta(E - \omega_s). \tag{11}$$

Fundamental quantities in linear-response theory are the (longitudinal) dielectric function ϵ and its inverse ϵ^{-1} (Refs. 3 and 31). In order to discuss them, we remind ourselves of the Kohn-Sham system: consider a set of noninteracting electrons subject to a Hartree potential and an exchange-correlation potential V_{xc}, chosen so that the charge density of this fictitious system and of the real system are identical.[1,32] The presence of an external potential induces charge redistribution and polarization in the Kohn-Sham system, which results in partial screening of the applied potential δV_{ext}. For a time-varying external perturbation, electrons are subject to an effective perturbation potential given by

$$\delta V_{eff}[\rho](1) = \delta V_{ext}(1) + \delta V_{SCF}[\rho](1),$$

where the self-consistent field is affected indirectly via charge density, $\delta V_{SCF} = V \delta \rho + \frac{\delta V_{xc}}{\delta \rho} \delta \rho$.[28] Defining the inverse dielectric function as the change in effective potential due to an external perturbation (Refs. 3 and 31),

$$\epsilon^{-1}(1,2) = \frac{\delta V_{eff}(1)}{\delta V_{ext}(2)},$$

we then obtain a relationship between inverse dielectric function and polarizability:

$$\epsilon^{-1}(1,2) = \delta(1,2) + \int (3) d(3) \left[V(1,3) + \frac{\delta V_{xc}(1)}{\delta \rho(3)} \right] \Pi(3,2).$$

In frequency representation, and using TDLDA for the exchange-correlation potential V_{xc}, the above equation reduces to

$$\epsilon_f^{-1}(\mathbf{r}, \mathbf{r}'; E) = \delta(\mathbf{r}, \mathbf{r}') + \int d\mathbf{r}'' [V(\mathbf{r}, \mathbf{r}'')$$
$$+ f_{xc}(\mathbf{r}) \delta(\mathbf{r} - \mathbf{r}'')] \Pi_f(\mathbf{r}'', \mathbf{r}'; E). \tag{12}$$

Along similar lines, the dielectric function ϵ is given by

$$\epsilon_f(\mathbf{r}, \mathbf{r}'; E) = \delta(\mathbf{r}, \mathbf{r}') - \int d\mathbf{r}'' [V(\mathbf{r}, \mathbf{r}'')$$
$$+ f_{xc}(\mathbf{r}) \delta(\mathbf{r} - \mathbf{r}'')] \chi_0(\mathbf{r}'', \mathbf{r}'; E), \tag{13}$$

where χ_0 is the irreducible polarizability operator, within the random-phase approximation (RPA) (Refs. 31 and 33):

$$\chi_0(\mathbf{r}, \mathbf{r}'; E) = 2 \sum_s \varphi_v(\mathbf{r}) \varphi_c(\mathbf{r}) \varphi_v(\mathbf{r}') \varphi_c(\mathbf{r}')$$
$$\times \left[\frac{1}{E - \varepsilon_c + \varepsilon_v + i0^+} - \frac{1}{E + \varepsilon_c - \varepsilon_v - i0^+} \right]. \tag{14}$$

Equations (12) and (13) describe screening of the external scalar field *and* of the induced field. Recently, Eq. (13) was used to calculate the TDLDA static screening in silicon clusters from first principles.[34] The importance of Eq. (12) is that it provides a direct relationship between polarizability and inverse dielectric function. For completeness, we present expressions for the dielectric function and its inverse within the RPA:

$$\epsilon_0^{-1}(\mathbf{r}, \mathbf{r}'; E) = \delta(\mathbf{r}, \mathbf{r}') + \int d\mathbf{r}'' V(\mathbf{r}, \mathbf{r}'') \Pi_0(\mathbf{r}'', \mathbf{r}'; E),$$
$$\tag{15}$$

$$\epsilon_0(\mathbf{r}, \mathbf{r}'; E) = \delta(\mathbf{r}, \mathbf{r}') - \int d\mathbf{r}'' V(\mathbf{r}, \mathbf{r}'') \chi_0(\mathbf{r}'', \mathbf{r}'; E), \tag{16}$$

where Π_0 is the RPA polarizability, evaluated from Eqs. (2)–(4) after setting $f_{xc} = 0$.

B. Electronic self-energy

A key quantity in solving the Bethe-Salpeter equation for optical excitations is the electronic self-energy Σ, which can be computed from first principles within the GW approximation (GWA).[2–4] The basis of this approximation lies in the so-called "Hedin equations," a set of nonlinear many-body equations which relate the self-energy with Green's function G, polarizability χ, screened Coulomb potential W, and vertex function Γ (Ref. 3):

$$W(1,2) = V(1,2) + \int d(34)V(1,3)\chi(3,4)W(4,2), \quad (17)$$

$$\chi(1,2) = -i \int d(34)G(1,3)G(4,1^+)\Gamma(3,4;2), \quad (18)$$

$$\Sigma(1,2) = i \int d(34)G(1,3)W(4,1^+)\Gamma(3,2;4), \quad (19)$$

$$\Gamma(1,2;3) = \delta(1,2)\delta(1,3)$$
$$+ \int d(4567)\frac{\delta\Sigma(1,2)}{\delta G(4,5)}G(4,6)G(7,5)\Gamma(6,7;3). \quad (20)$$

The approach taken by Hedin essentially generates a perturbation series in the screened interaction W. This expansion is expected to converge faster than an expansion in powers of the bare Coulomb potential V, as long as electronic screening is strong. Following this assumption,[3] the self-energy in Eq. (20) is first taken as zero and the vertex function reduces then to a delta function:

$$\Gamma(1,2;3) \approx \delta(1,2)\delta(1,3).$$

With that vertex function, the polarizability χ reduces to the RPA (Ref. 3):

$$\chi(1,2) \approx -iG(1,2^+)G(2,1) \equiv \chi_0(1,2).$$

The screened Coulomb interaction is evaluated in terms of the dielectric function. From Eq. (17), one gets:

$$\epsilon_0(1,2) = \delta(1,2) - \int d(3)V(1,3)\chi_0(3,2),$$

$$W_0(1,2) = \int d(3)\epsilon_0^{-1}(1,3)V(3,2)$$
$$= V(1,2) + \int d(34)V(1,3)\Pi_0(3,4)V(4,2),$$

and the self-energy is

$$\Sigma(1,2) = iG(1,2)W_0(2,1^+). \quad (21)$$

The first *ab initio* calculations of self-energies for semiconductors[2,35] followed the method outlined above. For periodic systems, the dielectric function can be conveniently expanded in a plane-wave basis and numerically inverted. Matrix inversion is a reasonably inexpensive step when the plane-wave expansion has a few hundreds or thousands of components. Dynamical effects can be included for instance by inverting the dielectric function at some values of frequency and either performing numerical integration over the

frequency axis,[4,35] or using a generalized plasmon pole model.[2]

On the other hand, numerical inversion of the dielectric matrix in real space is problematic because of the size of the matrix. As an example, a converged calculation for the ground state of the silane molecule (SiH_4) requires a real-space grid containing about 10^5 points.[34] Inverting the dielectric function in real space would require inverting a dense matrix of size $10^5 \times 10^5$. Although straightforward, this task requires an extremely large amount of floating point operations and CPU memory. This is certainly an extreme situation, but it illustrates the type of problems involved with straight matrix inversion. The same issue is present in periodic systems with large periodic cells: since the number of plane-wave components in a Fourier expansion is proportional to the volume of the cell, direct matrix inversion of ϵ is also numerically expensive.

Significant numerical simplification is achieved by working in the representation of single-electron transitions,[36] instead of using plane-wave or real-space representations for the dielectric function. There are two major advantages in doing that: the space of transitions is often much smaller than either the real space or reciprocal space, leading to matrices of reduced size; and integrations over frequency can be performed analytically since the polarizabilities χ_0 and Π_0 have known pole structure. In the space of transitions, a matrix element of the self-energy between Kohn-Sham orbitals j and j' is given schematically by:

$$\langle j|\Sigma(E')|j'\rangle = \langle j|i \int \frac{dE}{2\pi}e^{-iE0^+}G(E'-E)[V+V\Pi_0(E)V]|j'\rangle. \quad (22)$$

The integral above can be replaced with a sum over poles below the real energy axis. Following Hedin,[3,37] we write it as a summation of two terms: a bare exchange contribution Σ_x and a correlation contribution Σ_c,

$$\langle j|\Sigma_x|j'\rangle = -\sum_n^{occ.} K_{njnj'}^x, \quad (23)$$

$$\langle j|\Sigma_c(E)|j'\rangle = 2\sum_n \sum_s \frac{V_{nj}^s V_{nj'}^s}{E - \varepsilon_n - \omega_s \eta_n}, \quad (24)$$

where

$$V_{nj}^s = \sum_{vc} K_{njvc}^x \left(\frac{\varepsilon_c - \varepsilon_v}{\omega_s}\right)^{1/2} X_{vc}^s. \quad (25)$$

The derivation of Eqs. (23)–(25) from Eq. (22) is outlined in Appendix A. Whereas the summation over n in Eq. (23) is performed over all occupied Kohn-Sham orbitals, Eq. (24) has a summation over occupied and unoccupied orbitals. One can accelerate convergence in the last summation by truncating it and evaluating the remainder under the static approximation (see Appendix B). The coefficient η_n has the value $+1$ for unoccupied orbitals and -1 for occupied orbitals. In the equations above, eigenvectors X and eigenvalues ω are still evaluated under the random-phase approximation, ob-

tained by setting $f_{xc}=0$ in Eq. (4). In the following discussion, we refer to this level of approximation for the self-energy as GW_0.

At this point, it is natural to advance one step further and use dielectric screening within TDLDA instead of RPA. The impact of TDLDA screening in the context of the GW approximation in bulk silicon has been analyzed before.[2,24,38] In order to have a controlled level of approximation in Hedin's equations, we return to Eq. (20) and start an iterative solution by assuming $\Sigma(1,2) \approx V_{xc}(1)\delta(1,2)$. The vertex function then becomes

$$\Gamma(1,2;3) \approx \delta(1,2)\delta(2,3) + \int d(45)$$

$$\times [-i\delta(1,2)f_{xc}(1)]G(1,4)G(5,1^+)\Gamma(4,5;3).$$
$$(26)$$

The irreducible polarizability χ is now

$$\chi(1,2) = \chi_0(1,2) + \int d(3)\chi_0(1,3)f_{xc}\chi(3,2). \quad (27)$$

For the screened Coulomb interaction, we write Eq. (17) in terms of the full polarizability operator:

$$W(1,2) = V(1,2) + \int d(34)V(1,3)\Pi(3,4)V(4,2),$$

with

$$\Pi(1,2) = \chi(1,2) + \int d(34)\chi(1,3)V(3,4)\Pi(4,2).$$

From Eq. (27), we get

$$\Pi(1,2) = \chi_0(1,2) + \int d(34)\chi_0(1,3)[V(3,4)$$

$$+ f_{xc}(3)\delta(3,4)]\Pi(4,2).$$

Although written in real-space representation, the function Π above is identical to Eq. (2), and we refer to it as Π_f in the subsequent discussion. This function describes polarization due to an external potential accompanied by dynamical screening produced by the self-consistent field. Finally, we arrive at the following expression for the self-energy:

$$\Sigma(1,2) = iG(1,2)\left[V(1^+,2) + \int d(34)\{V(1,3)\right.$$

$$\left. + f_{xc}(1)\delta(1,3)\}\Pi_f(3,4)V(4,2)\right]. \quad (28)$$

We note that the use of TDLDA screening in the self-energy causes the inclusion of a vertex term (the second term inside curly brackets above). This level of approximation has been used before in the study of the quasiparticle band structure of crystalline silicon.[38] Equation (28) is a valid approximation for the self-energy but it is not symmetric with respect to the interchange of indices 1 and 2. In principle, this symmetry is not present in Eq. (19), but it can be recovered by defining a "left-sided" vertex function written schemati-
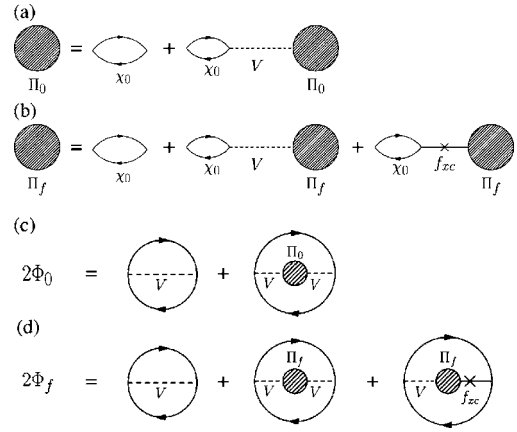

FIG. 1. Feynman diagrams for the polarizability operator Π (a), (b) and the function Φ (c), (d). The local exchange-correlation kernel is represented by a crossed line. Solid oriented lines are Green's functions. Dashed lines denote the bare Coulomb potential.

cally as $\Sigma=i\Gamma WG$ as opposed to $\Sigma=iGW\Gamma$ [c.f. Eq. (19)].[31] This deficiency is corrected by symmetrizing the last term in Eq. (28). Schematically, we rewrite $\Sigma=iG[V+V\Pi_f V + f\Pi_f V]$ as $\Sigma=iG[V+V\Pi_f V + \frac{1}{2}V\Pi_f f + \frac{1}{2}f\Pi_f V]$. Matrix elements of the self-energy are then given by:

$$\langle j|\Sigma(E')|j'\rangle = \langle j|i\int \frac{dE}{2\pi}e^{-iE0^+}G(E'-E)$$

$$\times \left[V + V\Pi_f(E)V + \frac{1}{2}V\Pi_f(E)f_{xc}\right.$$

$$\left. + \frac{1}{2}f_{xc}\Pi_f(E)V\right]|j'\rangle. \quad (29)$$

This self-energy operator is written as a sum of three contributions: $\Sigma=\Sigma_x+\Sigma_c+\Sigma_f$, where the first two terms are given by Eqs. (23) and (24) respectively, but now with full TDLDA screening ($f_{xc}\neq 0$). The last term is a vertex correction:

$$\langle j|\Sigma_f(E)|j'\rangle = \sum_n \sum_s \frac{V_{nj}^s F_{nj'}^s + F_{nj}^s V_{nj'}^s}{E - \varepsilon_n - \omega_s \eta_n}, \quad (30)$$

with

$$F_{nj}^s = \sum_{vc} K_{njvc}^{LDA}\left(\frac{\varepsilon_c - \varepsilon_v}{\omega_s}\right)^{1/2} X_{vc}^s. \quad (31)$$

In order to make a distinction between the two levels of approximation, we refer to the last approximation (Eq. (29)) as GW_f, as opposed to GW_0, Eq. (22).

It is not unexpected that, by using a polarizability function from TDLDA, we obtain a self-energy operator that has vertex corrections. In the language of many-body physics, the assumption in Eq. (26) implies that additional Feynman diagrams are included in the polarizability and in the self-energy. Figure 1(a) and 1(b) shows the diagrams included in the polarizability Π for both RPA and TDLDA. Although such diagrams include the LDA kernel, which does not have expansion in G and V, we can still define a many-body func-

tion Φ such that $\Sigma(1,2)=\delta\Phi/\delta G(1,2)$. The diagrams for Φ are depicted in Figs. 1(c) and 1(d). Adding the last diagram in Fig. 1(b) amounts to enhanced screening, since it allows for a new channel for electrons to redistribute in the presence of an external potential. This is counterbalanced by the inclusion of a vertex diagram [the right-most diagram in Fig. 1(d)]. We also note that Fig. 1 provides a justification for symmetrizing Eq. (28): differentiating the additional vertex diagram with respect to G leads to a pair of diagrams consistent with Eq. (30).

Inclusion of self-energy corrections in the description of the electronic system is done following the usual procedure: we assume the quasiparticle approximation and write down an eigenvalue equation for quasiparticles (Refs. 2 and 4),

$$[H_{LDA} + \Sigma - V_{xc}]\psi_j = E_j\psi_j, \tag{32}$$

where quasiparticle orbitals ψ_j are expanded in the basis of Kohn-Sham eigenfunctions and H_{LDA} is the (diagonal) LDA Hamiltonian.[4] Quasiparticle energies and wave functions are now found by direct diagonalization of the equation above.

In writing Eq. (32), we should consider carefully the energy dependence of Σ. Hybertsen and Louie[2] have shown that evaluating the self-energy around the quasiparticle energy leads to accurate band structures for cubic semiconductors. Since the quasiparticle energy is not known before Eq. (32) is solved, the suggested procedure[2] is to evaluate the operator $\langle\Sigma(E)-V_{\text{xc}}\rangle$ and its energy derivative at the LDA eigenvalue, $E=E_{\text{LDA}}$, and use linear extrapolation for the actual quasiparticle energy. We follow a similar methodology: first, we evaluate the diagonal part of the quasiparticle Hamiltonian in Eq. (32) and obtain a first estimate for quasiparticle energies by solving the equation $E_j=\varepsilon_j+\langle j|\Sigma(E_j)-V_{\text{xc}}|j\rangle$. In the next step, we include off-diagonal matrix elements and proceed through full diagonalization. At the end, quasiparticle energies are still close to their first estimate.

An open issue regarding the GW method is whether self-consistency between self-energy, polarizability and Green's function should be imposed or not and, if so, how to do it.[39] When the GW_0 and GW_f approximations were obtained by iterating Hedin's equations, self-consistency was lost and the vertex function was drastically simplified. Early work has indicated that self-consistency and vertex contributions partially cancel each other,[40] which may explain the remarkable success of the GW method for semiconductors. There have been some attempts at imposing partial self-consistency between self-energy and Green's function,[2,4] which resulted in quasiparticle energies improved by a fraction of an electron volt. Nevertheless, full self-consistency between self-energy and Green's function was observed to degrade the quasiparticle bandwidth and the description of the satellite structure in the electron gas.[41] In the subsequent applications, we do not attempt to impose self-consistency. Instead, the single-particle Green's function is always constructed from Kohn-Sham eigenvalues and eigenfunctions.

C. Bethe-Salpeter equation

While the GW method provides a description of quasiparticles in the system (i.e., the energy needed to add or extract one electron from the system), the solution of the Bethe-Salpeter equation gives information about neutral excitations: the process of promoting electrons from occupied quasiparticle orbitals to unoccupied ones. The important Green's function now is no longer the one-electron Green's function but the two-particle or, more specifically, the electron-hole Green's function.[31]

We start with a many-body expression for the polarizability:

$$\Pi(1,2) = -iL(1,2;1^+,2^+), \tag{33}$$

where L is the electron-hole correlation function,[7,8,31] which satisfies the Bethe-Salpeter equation:

$$
\begin{aligned}
L(1,2;&3,4)\\
&= G(1,4)G(2,3)\\
&+ \int d(5678)G(1,5)G(6,3)K(5,7;6,8)L(8,2;7,4).
\end{aligned}
\tag{34}
$$

The kernel operator K describes interactions between the excited electron and the "hole" left behind in the electron sea. The connection with GW is present in two aspects:

(i) The Green's function that enters in Eq. (34) is the Green's function for the interacting electronic system. Within the quasiparticle approximation, it is calculated with eigenvalues and wave functions obtained by diagonalizing Eq. (32).

(ii) The kernel K is related to the self-energy by (Refs. 7, 8, and 31):

$$K(1,2;3,4) = -i\delta(1,3)\delta(2,4)V(1,2) + \frac{\delta\Sigma(1,3)}{\delta G(4,2)}. \tag{35}$$

Although the functions G and K can be evaluated in many approximations, it is important to retain the same level of approximation in both quantities, so that all important Feynman diagrams are included and no diagrams are double-counted. In the lowest level of approximation, many-body effects can be ignored completely and the self-energy approximated by the LDA exchange-correlation potential, $\Sigma(1,2)\approx V_{\text{xc}}(1)\delta(1,2)$. In this case, the Green's function to be used is constructed from LDA eigenvalues and eigenfunctions, and Eq. (34) reduces itself to the TDLDA eigenvalue equation, Eq. (4). This fact has been explored in recent studies where model exchange-correlation functionals are designed to work as good approximations for the self-energy in Eq. (35) while retaining as much as possible the formal simplicity of TDLDA.[7,21,23] By its own nature, this family of approximations does not have Feynman diagrams in terms of which the self-energy is expanded.

Another level of approximation is GW_0, Eq. (22). The kernel K has then two terms: a bare exchange interaction, originated from the first term in Eq. (35), and a screened interaction, from $\delta\Sigma/\delta G=iW_0$. This approximation has been used in a variety of different applications with very good results (see, e.g., Refs. 7 and 8).

Finally, a third level of approximation is GW_f, Eq. (29). At this level, the kernel has an additional term besides the

previous two: a LDA vertex correction. As opposed to the kernel present in the TDLDA equation, the BSE kernel within either GW_0 or GW_f has explicit energy dependence, from the polarizability operator Π. This dependence was observed to be negligible when the interaction kernel itself is weak.[8] Ignoring dynamical effects and ignoring the mixing of absorption and emission contributions in the kernel,[94] one can rewrite Eq. (34) as an eigenvalue equation (Refs. 7 and 8):

$$(E_c - E_v)A_{vc}^l + \sum_{v'c'} (2K_{vcv'c'}^x + K_{vcv'c'}^d + K_{vcv'c'}^f)A_{v'c'}^l = \Omega_l A_{vc}^l, \tag{36}$$

where E_c, E_v are quasiparticle energies of unoccupied and occupied orbitals, respectively. The exchange kernel K^x has the same form given by Eq. (6). The kernels K^d and K^f are given by:

$$K_{vcv'c'}^d = K_{vv'cc'}^x + 4\sum_s \frac{V_{vv'}^s V_{cc'}^s}{\omega_s}, \tag{37}$$

$$K_{vcv'c'}^f = 2\sum_s \frac{V_{vv'}^s F_{cc'}^s + F_{vv'}^s V_{cc'}^s}{\omega_s}. \tag{38}$$

The eigenvectors A are normalized in the usual way, and the polarizability is now given by

$$\Pi_{BSE}(\mathbf{r},\mathbf{r}';E) = \sum_l \left[\frac{\rho_l(\mathbf{r})\rho_l(\mathbf{r}')}{E - \Omega_l + i0^+} - \frac{\rho_l(\mathbf{r})\rho_l(\mathbf{r}')}{E + \Omega_l - i0^+} \right], \tag{39}$$

with

$$\rho_l(\mathbf{r}) = \sum_{vc} \varphi_v(\mathbf{r})\varphi_c(\mathbf{r})A_{vc}^s. \tag{40}$$

As in the TDLDA, the solution of the Bethe-Salpeter equation provides the electrostatic susceptibility tensor and absorption cross section by equations analogous to (8), (9), and (11), with the replacements $\rho_s \rightarrow \rho_l$ and $\omega_s \rightarrow \Omega_l$.

D. Technical considerations

Working in the space of single-particle transitions has two clear advantages: it does not assume any particular boundary condition over electron wave functions, being equally valid for confined as well as extended systems; and it often leads to matrices smaller than the corresponding ones in real-space or reciprocal-space representations. In addition, the necessary numerical tasks are simple: matrix algebra (diagonalizations and matrix products), and evaluation of integrals of the type in Eqs. (6) and (7). We can also take advantage of existing point symmetries in the system at hand and divide the transition space into different group representations, resulting in block-diagonal matrices. This method can be readily extended to periodic systems by adding lattice periodicity as an additional symmetry operation. Each block is then associated to a particular k point in the Brillouin zone. For large systems, the solution of Eqs. (4) and (36) may involve large matrices, but further simplification is obtained by restricting the transition space to low-energy transitions. In the calculation of the self-energy terms Σ_c and Σ_f, one can proceed through the sum over single-particle states by including the static remainder (see Appendix B).

III. APPLICATIONS

In order to assess the reliability of the current implementation, we have employed it to study the excited-state properties of different classes of systems, both localized and extended. In all applications, we start from the electronic system in its ground state, as described within DFT. The exchange-correlation potential is used in the Ceperley-Alder form.[43] With the use of norm-conserving pseudopotentials,[44] we are able to remove core electrons from the problem, reducing considerably the numerical effort. In all applications, we use pseudopotentials constructed according to the Troullier-Martins prescription.[44] We employ a real-space approach in the solution of the Kohn-Sham equation.[45] In this approach, wave functions are expressed directly as functions of position. For a finite system, wave functions are required to vanish outside a spherical boundary with adjustable radius. The volume inside this boundary is sampled by a homogeneous grid with fixed grid spacing h along the three Cartesian directions. Results are tested for convergence with respect to the grid spacing and the boundary radius. We explore point symmetries both in the solution of the Kohn-Sham equation and in the calculation of integrals in Eqs. (6) and (7). For the self-energy operator, we include the static remainder according to Appendix B. We carefully test convergence with respect to the highest state explicitly included in the n summation. Except when noted, we compute self-energies at the GW_f level. Numerical accuracy in self-energy matrix elements is 0.2 eV or better. Excited states of the electronic system are calculated without the inclusion of effects due to structural relaxation.

A. Benzene and Naphthalene

Having a relatively small number of valence electrons makes the benzene molecule, C_6H_6, a good test system for the theory just presented. In addition, benzene has been the subject of extensive experiments, probing various properties such as linear optical response, electronic structure, and ionization.[46] On the theory side, its optical properties have been investigated with both TDLDA and GW-BSE approaches.[20,26,47] Quasiparticle energy levels of benzene and other oligoacenes have also been recently calculated using a first-principles Gaussian orbital-based method as well as a tight-binding approach.[15] The series of oligoacenes, benzene being the first element, is a sequence of molecules composed of n co-joined aromatic rings, starting from $n=1$ (benzene), $n=2$ (naphthalene), etc. Oligoacene crystals have received renewed attention recently due to their potential use in organic thin film devices.[11,48]

In our calculations, we solve the Kohn-Sham equations on a regular grid with grid spacing 0.4 a.u. (the Bohr radius being 1 a.u.). Electronic wave functions were required to
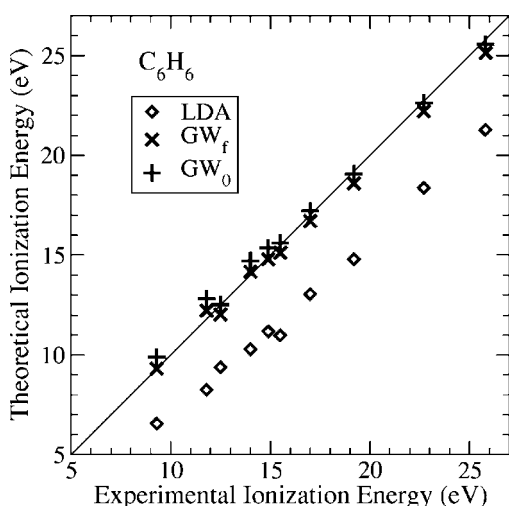
FIG. 2. Ionization energies of benzene, associated to all occupied orbitals in the molecule, as predicted within GW_0 and GW_f. The theoretical ionization energy is the negative of a quasiparticle energy eigenvalue. Experimental data from Ref. 54.

vanish outside a sphere of radius 16 a.u. centered on the molecule. Carbon-carbon and carbon-hydrogen bond lengths were fixed at their experimental values. The calculation of the self-energy operator was done including up to 305 unoccupied (virtual) orbitals in the TDLDA polarizability and in the calculation of correlation and vertex parts. This ensures that the sum rule is satisfied to within 30%, which was found to be sufficient for an accuracy of 0.1 eV in quasiparticle energies. After the self-energy operator was computed, quasiparticle energies for occupied and unoccupied orbitals were obtained by diagonalizing the Hamiltonian in Eq. (32). Extensive convergence tests have been performed on all relevant numerical parameters: choices of 0.3 and 0.4 a.u. were used for the grid spacing; we have used boundary radii of up to 20 a.u., and included up to 1000 virtual orbitals. For the last choice, the sum rule is satisfied to within 14%.

Figure 2 shows a comparison between theoretical and experimental ionization energies. In the framework of the GW approximation, the first ionization energy is interpreted as the negative of the quasiparticle energy for the highest occupied molecular orbital (HOMO). Higher ionization energies are obtained from deeper molecular orbitals. As a reference, we show in Fig. 2 the prediction from LDA (i.e., negative of the Kohn-Sham eigenvalues for occupied orbitals), although such comparison should be made with caution since, from a

strict point of view, such eigenvalues enter in DFT as mathematical entities, with no explicit physical meaning. By extending Koopman's theorem to DFT, the HOMO eigenvalue can be shown to be equal to the first ionization potential if the exact functional is used,[49] but such property does not hold for higher ionization potentials.[49,50] Hybrid functionals[51] and the ones of the exact-exchange type[52,53] can give very good predictions for the first ionization potential.

In contrast, quasiparticle energies do have physical meaning, and Fig. 2 shows definitive consistency between theory and experiment. In particular, the first ionization energy is predicted to be 9.30 eV within GW_f, with remarkable agreement with the experimental value of 9.3 eV (Refs. 46 and 54) and also with the prediction from quantum chemistry calculations: 9.04 eV.[55] A hybrid B3LYP functional predicts 9.74 eV for this ionization energy.[56] The GW_0 approximation predicts the same quantity to be 9.88 eV. The difference is due mostly to the vertex term: the contribution Σ_f for the HOMO alone is found to be almost 0.8 eV, while LDA exchange-correlation corrections in the polarizability give a contribution somewhat smaller but of opposite sign. For other quasiparticle energies, the vertex term is always positive (i.e., it lowers the ionization energy compared to the GW_0 value), and no more than 1 eV.

Ionization energies in the range of 20 to 25 eV are found to be systematically underestimated with respect to experiment, as shown in Fig. 2. For such deep orbitals, we expect to have some loss of numerical accuracy since, although the energy dependence of the polarizability Π_f is exactly calculated using Eq. (2), the summation over s is always limited to a finite number of poles.

The quasiparticle energy for the lowest unoccupied molecular orbital (LUMO) is the negative of the electron affinity,[3,8] and its calculated value is shown in Table I. Although the anion $C_6H_6^-$ is unstable, Burrow and collaborators[58] have been able to perform careful electron transmission experiments and identify resonances in the spectrum, which where associated to the electron affinity. Two resonances where found: at energies 1.12 and 4.82 eV. They match theoretical predictions from the GW_f approximation both in energy and spacial distribution: $e_{2u}(\pi^*)$ and $b_{2g}(\pi^*)$, respectively. Again, there is a discrepancy between GW_0 and GW_f quasiparticle energies of about 0.5 eV, mostly due to vertex corrections in the self-energy.

If measuring electron affinities of benzene is not trivial, a similar statement can also be made regarding first-principles calculations. The anion $C_6H_6^-$ is correctly predicted within

TABLE I. Electron affinities in benzene, as predicted within GW_0 Eq. (22) and GW_f Eq. (29). The outer-valence Green's function (OVGF) method[55] is based on a Hartree-Fock expansion of the self-energy, combined with self-consistent calculations of self-energy and Green's function. All energies in eV.

	LDA	GW_0	GW_f	DFT(B3LYP)[a]	OVGF[b]	Exp.[c]
e_{2u}	1.33	−0.47	−0.99	−0.88	−2.605	−1.12
b_{2g}	−2.45	−4.49	−5.05			−4.82

[a]Reference 57.
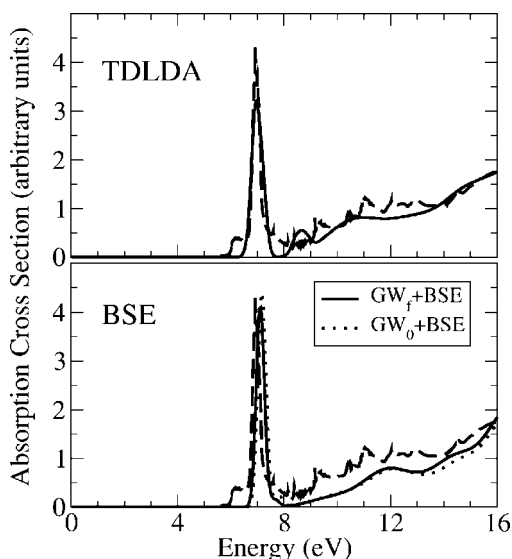[b]Reference 55.
[c]Reference 58.

FIG. 3. Absorption spectrum of benzene, modified from numerical results published in Ref. 26. Results from both, TDLDA (upper panel) and BSE (lower panel) methods are shown. Absorption lines were broadened by Gaussian convolution with dispersion 0.15 eV (below 10 eV) and 0.5 eV (above 10 eV). The measured spectrum (Ref. 61) is shown by the dashed lines. In the lower panel, the BSE was solved using two approximations for the self-energy: GW_0 (dotted line) and GW_f (solid line).

DFT to be unstable, and methods such as ΔSCF (energy variations in self-consistent field) fail to predict its electron affinity.[26] Indeed, confining the anion inside a spherical boundary of radius R and solving the Kohn-Sham equations results in an excess energy relative to the neutral system that is proportional to R^{-2}. This excess energy vanishes in the limit of a very large radius. The physical picture is that, although the anion is unstable, it can be detected as a resonance if electrons do not remain in their ground state, and the GW approximation predicts that resonance as a quasiparticle orbital.

As mentioned in the context of Eq. (32), quasiparticle wave functions are obtained by numerically diagonalizing the quasiparticle Hamiltonian, and therefore they are different from Kohn-Sham eigenfunctions. For the benzene molecule, we observed though that quasiparticle and Kohn-Sham

eigenfunctions overlap by more than 95% for all occupied orbitals. This is due to the high symmetry of the benzene molecule, which makes most off-diagonal matrix elements of the self-energy zero by selection rules. Similarly, the resonant states e_{2u} and b_{2g} in Table I have overlaps of 99 and 63%, respectively. For them, overlap is still suppressed by selection rules but the existence of many low-energy, unbound orbitals makes overlap somewhat more favorable for orbitals well above the HOMO-LUMO gap.

Optical excitations were obtained in two methods: both within TDLDA and by solving the BSE. Figure 3 shows the cross section for photoabsorption in benzene. It is dominated by a sharp and well pronounced peak at around 7 eV, as verified by various calculations.[20,47,59,95] This peak is the visible component of a π-π^* complex, originated from transitions between the HOMO and the quasiparticle state e_{2u}. The low, flat feature in the 6.0–7.0 eV range is due to coupling between π-$\pi^{\ddagger}$ transitions and vibrational modes,[47,60] and it is absent in the calculated spectra because of the assumed structural rigidity. Beyond 10 eV, a number of sharp features in the measured spectrum results from transitions involving Rydberg states.[60,61] The limited numerical accuracy in that energy range prevents a detailed identification of such transitions in the calculated spectrum.

Table II shows a comparison between TDLDA and BSE predictions for some excitations in the π-$\pi^{\ddagger}$ complex, together with CASPT2 calculations[62] and other TDDFT calculations.[52,63] Although singlet transitions B^1_{1u} and E^1_{1u}, which are the dominant ones in the low-energy part of the absorption spectrum, are equally well described by both methods, there is a significant blueshift of dark transitions B^3_{1u} and B^1_{2u} within all TDDFT approaches presented. With the exception of the E^1_{1u} transition, excitation energies obtained by solving the BSE are typically underestimated with respected to measured quantities. The overall deviation between measured transition energies and GW predictions is 0.1 to 0.3 eV, comparable to CASPT2 results.[62]

Although excited states can be obtained from either TDLDA or BSE by solving suitable eigenvalue problems, these two theories provide very different descriptions for "electron-hole" correlations. Within TDLDA, such correlations are included in the exchange-correlation kernel, which is static and local in space. Within BSE, they are included both in quasiparticle energies (through the self-energy opera-

TABLE II. Excitation energies of the lowest-energy neutral excitations in benzene. Energies in eV.

	TDLDA	GW_0+BSE	GW_f+BSE	TDDFT(B3LYP)[a]	TDDFT(LHFX)[b]	CASPT2[c]	Exp.[d]
Triplet							
B_{1u}	4.53	3.59	3.59	4.45	4.27	3.89	3.9
Singlet							
B_{2u}	5.40	4.74	4.86	5.24	5.40	4.84	5.0
B_{1u}	6.23	6.08	6.14	6.09	6.12	6.30	6.2
E_{1u}	6.9–7.2	7.16	7.23	6.90	6.96	7.03	6.9

[a]Reference 63.
[b]Reference 52.
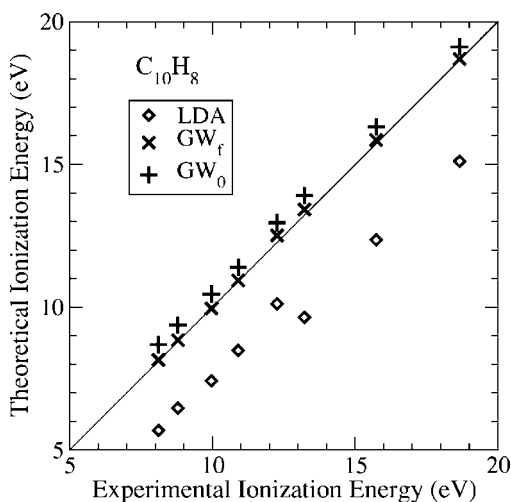[c]Reference 62.
[d]Reference 64.

FIG. 4. Ionization energies of naphthalene, associated to all occupied π orbitals and the first σ orbitals in the molecule. Experimental data from Ref. 67.

tor) and in the kernels K^d and K^f. And these differences manifest themselves in a very intriguing way in the π-π^* complex: both theories agree within 0.1 eV in the excitation energy of components B_{1u} and E_{1u}, but they differ by more than 0.5 eV in the excitation energy of component B_{2u}.

As observed in Fig. 2 and Table I, the inclusion of vertex corrections together with a TDLDA polarizability is essential for an accurate prediction of the ionization potential and electron affinity of benzene. In fact, the GW_0 approximation predicts those quantities to be 9.84 and −0.54 eV, respectively. Defining a "HOMO-LUMO gap" as the difference between ionization potential and electron affinity, both GW_0 and GW_f approaches agree in the value of the gap: 10.3 eV. This is somewhat consistent with the observation by del Sole and collaborators,[38] who conducted a similar analysis in bulk silicon and found significant shifts in the valence band maximum and conduction band minimum, but only a small change in the energy gap itself. Due to the cancellation of vertex contributions, the energy position of the π-π^* line is not significantly affected by the choice of self-energy approximation in the solution of the BSE, as shown in the lower panel of Fig. 3.

Naphthalene, $C_{10}H_8$ is the second smallest oligoacene. For this molecule, we used the following parameters in the solution of the Kohn-Sham equation: grid spacing 0.4 a.u., boundary radius 20 a.u., and experimental values of bond length. Ionization potentials associated to all occupied π orbitals and some σ orbitals were reported by Dewar and Worley,[67] with the first one being 8.11 eV.[67] Some of the theoretical calculations of the first ionization potential are: 7.85 eV (OVGF method[55]); and 7.59 eV (hybrid B3LYP/DFT[68]). Predictions from the GW_f and GW_0 approximations are 8.15 and 8.69 eV, respectively. Figure 4 presents a comparison between the predictions from the GW_f and GW_0 approximations for all other potentials. Although both are acceptable, the GW_f approximation is clearly superior to GW_0, giving a maximum deviation from experiment of no more than 0.3 eV. Vertex corrections are of the order of 0.6 eV. We should point out that the magnitude of self-energy corrections for π orbitals (experimental ionization energy ranging from 8 to 13 eV[67]) is around 2.4 eV, whereas the self-energy corrections for σ orbitals (experimental ionization energy ranging from 13 to 19 eV[67]) is bigger: around 3.6 eV. Since σ orbitals are typically deeper in energy than π, they are expected to have self-energy corrections larger in magnitude.

There has been some debate in the literature concerning the stability of the anion $C_{10}H_8^-$ (Ref. 69) Early electron capture experiments have observed a stable anion with electron affinity in the range of 0.15 eV.[70] In contrast, electron transmission spectroscopy measurements have indicated the ion to be unstable, with negative electron affinity of −0.2 eV.[58] The anion is predicted by GW_f to be stable, with an electron affinity of 0.14 eV. Table III presents a comparison between the calculated electron affinities and the experimental data.[58] The fact that the anion has such small binding energy makes any stability analysis, either from theory or experiment, very difficult. As observed in benzene, there is a number of low-energy orbitals around the LUMO, most of them highly delocalized. But some of those orbitals are localized around the molecule, and they are responsible for the resonant states detected in electron transmission spectroscopy measurements.[58] For the resonant states, we find fair agreement in terms of orbital character and corresponding electron affinity, although there is a discrepancy of typically 0.2 to 0.3 eV in the last quantity.

The absorption spectrum of naphthalene is found to have a sharp and well-pronounced line at 6.0 eV. This line is originated from a B_{1u} transition which is optically active for light polarization along the line that joins the centers of the two aromatic rings in the molecule, called "long molecular axis." A second, lower absorption line is located at 4.3 eV and it has B_{2u} character, being highly active for polarization

TABLE III. Electron affinities in naphthalene. Energies in eV.

	LDA	GW_0	GW_f	DFT(B3LYP)[a]	OVGF[b]	Exp.[c]
b_{1g}	1.38	−0.09	−0.60			−0.90
b_{2g}	2.19	0.64	0.14	−0.20	−1.30	−0.19
b_{3u}	0.76	−1.07	−1.35			−1.67
a_u	−1.14	−3.03	−3.44			−3.38

[a]Reference 57.
[b]Reference 55.
[c]Reference 58.

TABLE IV. Excitation energies of the lowest-energy neutral excitations in naphthalene. Spin-singlet states only. Energies in eV.

	TDLDA	GW_0+BSE	GW_f+BSE	TDDFT(B3LYP)[a]	CASPT2[b]	Exp.[c]
B_{1u}	4.40	3.93	4.02	4.21	4.03	3.97
B_{2u}	4.32	4.28	4.34	4.12	4.56	4.45
B_{1u}	5.84	6.04	6.12	5.69	5.54	5.89
B_{2u}	6.13	6.08	6.16	5.90	5.93	6.14

[a]Reference 63.
[b]Reference 65.
[c]Reference 66.

on the plane of the molecule but perpendicular to the long molecular axis. TDLDA and BSE give very similar values for the energy position of both lines, although they differ by 0.5 eV in the predicted value of the first excited state, a dark B_{1u} singlet excitation. A comparison between the theoretical calculations and experimental data is shown in Table IV.

In summary, the absorption spectra of benzene and naphthalene are dominated by a sharp π-π^* transition, found in both TDLDA and GW+BSE methodologies. Considering that this transition is composed of hybridized carbon-p orbitals, it is expected to be very localized in space. We do not discard the possibility of strong spacial localization being a major reason for such good agreement between TDLDA and GW+BSE, despite the conceptual simplicity of the former. The good agreement between predicted and measured ionization potentials of benzene and naphthalene is equally remarkable. There has been a very limited number of cases where such quantities were calculated within the framework of the GW approximation,[4,8,9,17–19] and the present results provide the first benchmarks for ionization potentials in oligoacenes.

B. Silicon clusters

Small semiconductor clusters containing a few tens of atoms and with various chemical compositions have been mass produced and characterized in terms of their optical properties and structural configuration, although the synthesis of small silicon clusters remains a challenging task.[14,71,72] From a theoretical point of view, optical properties of small silicon clusters are interesting for one aspect: the linear optical spectrum of bulk silicon is known to be extremely well predicted by a first-principles approach based on the BSE,[7,8] whereas TDLDA fails to predict both the optical gap and excitonic effects.[21,73,96] On the other hand, optical excitations of SiH_4 and Si_2H_6, the two smallest "clusters," are correctly described within TDLDA.[20] Based on these two facts, it is natural to investigate what limits the validity of each theory and where the crossover size is, beyond which one theory becomes superior to the other. Such an analysis is challenging because of two major factors: the limited number of useful experiments, and the complexity of some numerical implementations of the BSE method. Recently, a study based on model dielectric screening in silicon clusters have addressed the issue, with inconclusive results.[18] Since the present implementation of the BSE method is particularly efficient for finite systems, we are able to compare both

TDLDA and BSE methods in a wide range of cluster sizes and with a minimum of *ad hoc* assumptions. As we discuss below, there is unfortunately one additional difficulty in such comparisons: there is no direct relationship between the optical spectrum of a nanostructure (quantified by the absorption cross section, for instance) and the optical spectrum of a macroscopic solid (quantified by the macroscopic dielectric function).

In general, the surface of synthesized silicon clusters is covered by passivating particles and, for the smallest ones, they may undergo significant reconstruction.[72] Our approach is to construct clusters from fragments of crystalline silicon and adjust the number of atoms so that the fragment has surface as spherical as possible. Dangling bonds on the surface are passivated by attaching hydrogen atoms. We do not consider surface reconstruction. Although the class of tetrahedral clusters we discuss here may not be the most stable ones in the size range of 0 to 2 nm, they are expected to be the most stable ones when the cluster size is very large. Here, we analyze the clusters SiH_4, Si_5H_{12}, $Si_{10}H_{16}$, $Si_{14}H_{20}$, $Si_{29}H_{36}$, $Si_{35}H_{36}$, $Si_{47}H_{60}$, $Si_{71}H_{84}$, $Si_{99}H_{100}$, and $Si_{147}H_{100}$. Since the presence of hydrogen atoms typically requires dense grids, we use grid spacings ranging from 0.5 (SiH_4) to 0.7 a.u. ($Si_{147}H_{100}$) in the solution of the Kohn-Sham equations.

For each cluster, the quasiparticle Hamiltonian is reorthogonalized in the Kohn-Sham basis. As emphasized in the literature,[8,17] the self-energy operator is not diagonal, and Kohn-Sham eigenfunctions are not good approximations for quasiparticle wave functions, particularly for the low-energy unoccupied orbitals in the smallest clusters. There are two main reasons for this phenomenon: LDA wrongly predicts some of these unoccupied states to be bound, whereas quasiparticle orbitals are often unbound and more extended; and the large density of orbitals within a few eV from the LUMO makes the occurrence of non-negligible off-diagonal matrix elements of the operator in Eq. (32) very frequent. The $Si_{35}H_{36}$ cluster is a typical example. There, overlap between Kohn-Sham and quasiparticle wave functions is observed to be greater than 95% for most occupied states and for the first few unoccupied ones, but it reduces to values ranging from 30 to 90% for the higher-energy unoccupied states.

One important aspect involving self-energy corrections is whether they can be modeled by a "scissors" operator or not. Frequently, the quasiparticle band structure of solids differs from the one predicted within LDA by a rigid upward shift of conduction bands with respect to valence bands,[2,4] which
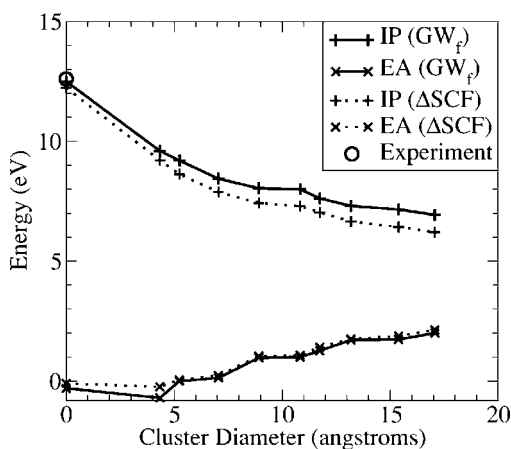
FIG. 5. First ionization potential and electron affinity of passivated silicon clusters, calculated within the GW_f approximation (solid lines) and ΔSCF (dotted lines). Experimental data from Ref. 71. ΔSCF results include spin-polarization effects.

justifies the scissors approximation. Scissors operators with energy dependence can also improve bandwidths.[4] But we find this procedure to be inaccurate even for moderately large clusters. Figure 6 shows diagonal matrix elements of the self-energy operator as a function of the LDA energy eigenvalue for all occupied orbitals and some unoccupied orbitals of $Si_{35}H_{36}$. For deep occupied orbitals, these matrix elements follow a quasicontinuous distribution, with smooth curvature, so a scissors operator could be defined. But the matrix elements for orbitals in the vicinity of the energy gap do not have a well-defined dependence with respect to LDA eigenvalues. On the contrary, they have a strong orbital dependence. This fact, together with the existence of large off-diagonal matrix elements, makes any attempt at constructing a scissors operator very difficult for these clusters.

Figure 5 shows the dependence of electron affinity and first ionization potential with respect to the cluster diameter. To our knowledge, the ionization potential has not been measured for any of the studied clusters except for SiH_4, for
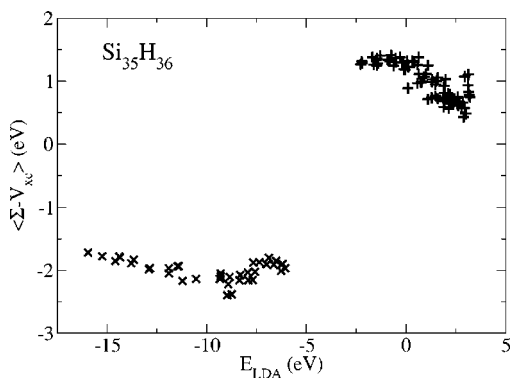

FIG. 6. Diagonal matrix elements of the operator $\Sigma - V_{xc}$, c.f. Eq. (32), evaluated on the basis of Kohn-Sham eigenfunctions. Matrix elements for occupied (unoccupied) orbitals are represented by crosses ("plus" signs). Self-energy is evaluated within the GW_f approximation and at the extrapolated quasiparticle energy (see the text).
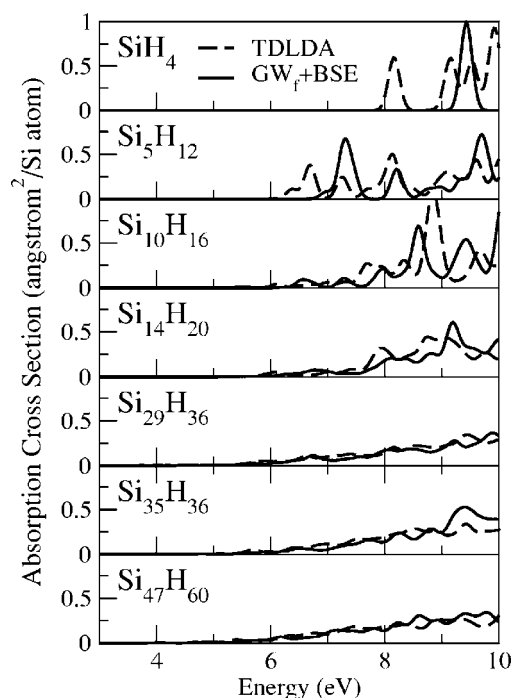

FIG. 7. Cross section for photoabsorption in passivated silicon clusters, calculated within TDLDA (dashed lines) and BSE (solid lines). The self-energy operator used in BSE is calculated within the GW_f approximation. The cross section is normalized by the number of silicon atoms in each cluster. Absorption lines were broadened by a Gaussian convolution with dispersion 0.1 eV.

which the experimental value is 12.6 eV.[71] For this system, the prediction from GW_f is 12.5 eV. Starting from SiH_4, the first ionization potential decreases monotonically as the cluster size increases. On the other hand, the electron affinity remains very small, with little dependence with respect to cluster size. As a result, the electronic gap (defined as the difference between ionization potential and electron affinity) decreases continuously for larger and larger clusters. This is a size effect which has been observed before for small clusters.[8] In order to understand the physics behind it, we model the cluster as an electron sphere with homogeneous density and radius R, keeping the density constant and proportional to N/R^3. The energy of the HOMO is found by integrating the density of states up to the number of electrons N, resulting in $E_F = const. \times N^{2/3}R^{-2}$. The energy difference between this orbital and the next one is approximately $\Delta E = const. \times N^{-1/3}R^{-2} = const. \times R^{-3}$, which is inversely proportional to the volume of the cluster. A more elaborate analysis predicts a power law R^{-2} instead of R^{-3} (Ref. 74).

We observe a systematic discrepancy in the first ionization potential as predicted within GW_f and ΔSCF, the difference being 0.6 to 0.9 eV throughout the range of studied cluster sizes. In contrast, the electron affinity shows better agreement between these two theories. Possible explanations for this behavior are the spurious self-interaction effect, present in ΔSCF calculations, and the incorrect asymptotic behavior of the LDA functional.[1,75]

Figure 7 shows the absorption cross section for clusters SiH_4 to $Si_{47}H_{60}$. The cross section also has a characteristic

behavior as a function of cluster size: for small clusters, it has a small number of well-defined peaks but, as size increases, their intensity decreases in the low end of the energy axis. For large clusters, the absorption cross section shows a smooth and featureless profile, with the onset at a low energy value and continuous increase towards higher values of energy. Also, TDLDA and BSE spectra are significantly different for small clusters. In particular, TDLDA predicts a $s \rightarrow p$ line at around 8.2 eV, whereas the $s \rightarrow p$ line in BSE is positioned at 9.4 eV. Previous BSE calculations have predicted 9.0 eV (Ref. 76) and 9.16 eV (Ref. 8) for the same quantity. The experimental value has been reported to be around 8.8 eV.[71] For bigger clusters, the differences between TDLDA and BSE tend to disappear.

As pointed out recently,[18] the behavior of the absorption cross section for large clusters is dictated by the exchange kernel $K^x_{vcv'c'}$, which is present in both TDLDA and BSE formalisms. This term introduces a long-range interaction that increases in strength as a function of cluster size and ultimately dominates both the exchange-correlation kernel in the TDLDA eigenvalue equation and the direct+vertex kernel in the BSE. As a result, oscillator strength is redistributed among the excited states of the system and the absorption spectrum peaks at frequencies well above the optical range. Differences in the detailed treatment of electron-hole correlations, intrinsic to both TDLDA and BSE, are expected to be less and less important for increasingly large clusters.

As the cluster size increases, more transitions become allowed and the absorption cross section is expected to evolve into a well-pronounced and broad peak at the plasmon-pole frequency. Indeed, the formalism in Secs. II A and II C can be applied directly to solids. In solids, Eq. (11) reduces to a function proportional to the imaginary part of the inverse dielectric function, measurable by electron energy loss spectroscopy, EELS. Olevano and Reining[77] have shown that the random-phase approximation correctly predicts the essential features of the EELS of bulk silicon, and including corrections at the BSE level does not lead to substantial improvements. As expected, the spectra of the largest clusters studied, depicted in the lower panels of Fig. 7, show a smooth profile typical of the low-energy end of the plasmon peak.

The blueshift can be discussed in terms of classical electrodynamics. We consider a material composed of several identical, spherical particles in suspension inside an optically inert background. According to the Mie theory (or *effective medium theory*),[25,78] the (macroscopic) dielectric function of the medium is size-dependent, and there are three important regimes: particles much smaller than the wavelength of light; particles of size comparable to the wavelength of light; and particles much bigger than the wavelength of light. In the regime of small particles in very low concentration, the imaginary part of the dielectric function is proportional to the absorption cross section of each particle according to the expression

$$\epsilon_2 = n\lambda\sigma/2\pi, \qquad (41)$$

where λ is the wavelength of light and n is the concentration. The two functions then share the same energy dependence. This is a special case of the Clausius-Mossotti relation when $n \rightarrow 0$. In denser medium, the proportionality above no longer holds and the energy dependence of ϵ_2 is now given by a nonlinear Clausius-Mossotti relation. In the extreme situation of highly packed particles, with no interstices, the function ϵ_2 should resemble the bulk dielectric function. As the particles condense, any similarity between the energy dependencies of ϵ_2 and σ is lost. The qualitative aspects of this analysis still hold for more complicated cases, such as nonspherical and/or inhomogeneous particles. Some predictions of the Mie theory for the optical properties of nanostructures have been discussed in recent first-principles calculations: the emergence of a Mie plasmon in nanoclusters;[79] and the dependence of dielectric function with respect to concentration in periodic arrangements of nanowires.[80]

In Fig. 7, the parameter is particle size rather than concentration. From the calculated spectra, one can recover the bulk limit by increasing the concentration or the size of particles. In the first case, the Mie theory predicts a redshift of ϵ_2 with respect to σ. The second case should certainly involve a similar phenomenon but it requires a more elaborate analysis, because of the crossover between the particle size and wavelength. The crossover does not necessarily affect the absorption cross section because light is not an essential element in absorption measurements (for instance, one can use electron beams instead of photons as a probe). But it should affect the dielectric function because measurements of dielectric function necessarily involve interaction with photons.

Although the behavior of the absorption cross section is well understood, we conclude that spectra of large clusters are not directly related to the macroscopic dielectric function. Whereas excitonic effects and optical band gaps are easily recognized in the macroscopic dielectric function, the same does not hold for the inverse dielectric function. In principle, these two functions are linked by simple inversion,[3,7,31] but the delicate features of both functions can be lost if numerical inversion is attempted without careful control of numerical accuracy. For solids, numerical inversion is avoided by replacing the BSE for the polarizability operator with a similar equation that, when solved, provides the macroscopic dielectric function directly.[7,81] For confined systems, no such prescription is known, and therefore the question of how to compute an absorption spectrum that, in the bulk limit, reduces unambiguously to the macroscopic dielectric function remains unanswered.

The problem of an indeterminate crossover and ill-defined bulk limit in the absorption spectrum has two important consequences. The first one is that the identification of excitonic effects in large silicon clusters becomes a nontrivial task, even if the cluster is sufficiently large so that the very concept of "exciton" applies. The second is that an optical gap cannot be easily extracted from the absorption cross section of large clusters. As seen in Fig. 7, the onset of absorption for the large clusters is not well defined. Often, low-energy excitations in the cluster have extremely small oscillator strength and they should not be used to define a gap. Presently, one tentative definition of the optical gap is via a threshold approach: the optical gap E_G is such that the integrated cross section up to E_G is a fixed fraction of the total integrated cross section (Ref. 20).
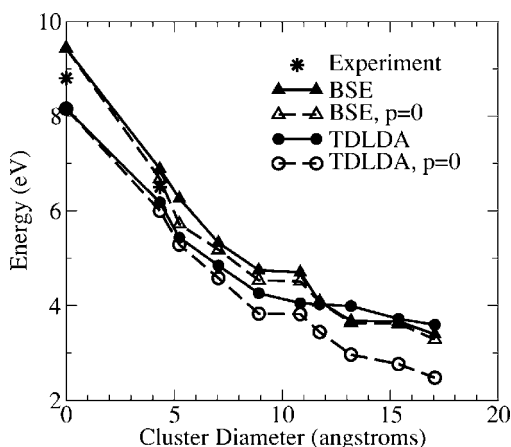
FIG. 8. Minimum gap (dashed lines and open symbols) and optical gap (solid lines and filled symbols) for passivated silicon clusters. Circles denote TDLDA gaps. Triangles denote GW_f +BSE gaps. The optical gap is obtained by integrating the oscillator strength up to $p=1\times10^{-4}$. The minimum gap is defined as the lowest spin-singlet excitation energy ($p=0$) in the system. Experimental data from Refs. 71 and 82.

$$\int_0^{E_G} \sigma(E)dE = p\int_0^\infty \sigma(E)dE, \qquad (42)$$

where p is a small fraction. This prescription is motivated by experiment: often, the onset of absorption cross section cannot be distinguished due to the limitations in experimental resolution, and a practical definition of an optical gap becomes important. An obvious drawback of Eq. (42) is that the gap may be sensitive to the choice of p. In practice, this prescription has been observed to be robust.[20]

In Fig. 8, we show the minimum gap and optical gap as predicted within TDLDA and BSE. The minimum gap is defined as the energy of the lowest excited state, irrespective of oscillator strength, whereas the optical gap is defined from Eq. (42) with $p=2\times10^{-4}$. As expected, both gaps have a strong dependence with respect to cluster size. In addition, the BSE gaps are typically larger than the corresponding TDLDA ones, the difference slowly decreasing for larger clusters and almost vanishing for $Si_{147}H_{100}$. Figure 8 also shows that the difference between the TDLDA minimum and optical gaps has a slow tendency towards increasing with cluster size, but the same is not observed in the BSE gaps. The reason for this behavior is that low-energy excitations obtained within BSE have larger oscillator strengths than the corresponding ones in TDLDA. Discrepancies between the TDLDA optical gap in Fig. 8 and previous work[20] is due to different choices for the value of p.

The dependence of the minimum gap with respect to cluster size has also been discussed in the context of quantum Monte Carlo (QMC) calculations.[83] QMC and GW+BSE share a common link: both of them are many-body theories, and therefore they both include correlation effects not present in TDLDA. A signature of these effects can be recognized in the calculated minimum gap: QMC and GW +BSE give similar values for that quantity, both of them

overestimated with respect to TDLDA (c.f. Fig. 8 and Ref. 83). For large clusters, there is a tendency for the QMC gap to fall above the GW+BSE gap. For instance, the GW +BSE minimum gap for $Si_{147}H_{100}$ is found to be 3.3 eV, whereas QMC predicts a gap of around 4 eV.[83] The corresponding gap within TDLDA is found to be 2.5 eV.

C. *F*-center defects in LiCl

The formalism presented in Sec. II B can also be applied to extended systems, once the appropriate boundary conditions are used in the solution of the Kohn-Sham equations.[84] In fact, the boundary conditions imposed on electron wave functions determine the ones for the polarizability operator Π, through Eqs. (2), (3), (39), and (40). In periodic systems, optical absorption is quantified by the absorption coefficient, or by the imaginary part of the macroscopic dielectric function. Here, we calculate this dielectric function following an approach due to Hanke.[7,81] The basis of this approach is in defining a truncated Coulomb potential $\hat{V}$ in the construction of the exchange kernel K^x:

$$K^x_{vcv'c'} \rightarrow \hat{K}^x_{vcv'c'} = K^x_{vcv'c'} - \frac{4\pi e^2}{N_k V_{cell}}\frac{\langle v|\lambda\cdot\mathbf{v}|c\rangle}{\varepsilon_c - \varepsilon_v}\frac{\langle c'|\lambda\cdot\mathbf{v}|v'\rangle}{\varepsilon_{c'} - \varepsilon_{v'}},$$

where $\lambda\cdot\mathbf{v}$ is the velocity operator projected along some direction λ. The volume of the periodic cell, V_{cell} and number of k points, N_k, are included as normalization factors. The kernel $\hat{K}^x$ in the above equation does not have direct physical meaning, being rather an auxiliary quantity, which differs from the original K^x by the absence of a long-range Coulomb interaction. By using this truncated kernel, Hanke has shown[81] that a polarizability operator can be obtained and, from that, the macroscopic dielectric function according to

$$Im\{\epsilon\} = \frac{4\pi^2 e^2}{N_k V_{cell}}\sum_s \frac{1}{\omega_s^2}\left|\int d\mathbf{r}\rho_s(\mathbf{r})\lambda\cdot\mathbf{v}\right|^2 \delta(E - \Omega_s),$$

$$(43)$$

where ρ_s and ω_s can be found by diagonalizing either TDLDA-like or BSE-like eigenvalue equations.[7,73,81] In addition, lattice periodicity allows us to use a wave vector $\mathbf{q}$ as an additional quantum number in the polarizability Π. Each choice of $\mathbf{q}$ leads to a different eigenvalue equation and the resulting partial polarizabilities are summed up.

Here, we are interested in analyzing the optical spectrum of an F center embedded in an otherwise ordered LiCl crystal. F centers are halogen vacancies found in alkali-halide crystals, and they are named after the bright, visible coloration they induce. Alkali-halide crystals are well-known for their strong ionicity and wide energy gap, which makes them transparent to visible light. Halogen vacancies induce localized electronic states inside the gap, and electronic transitions involving such localized states are the source of the bright color in F-center-rich crystals. The nature of F centers has been studied experimentally using various techniques.[85]

From a theoretical point of view, F centers are challenging because the exact location of defect states inside the gap is not easily obtained without experimental input. Effective-

TABLE V. Electron band structure of the F center in LiCl, with defect levels. All calculated energies are given with respect to the valence band maximum as predicted by GW_f, in eV. Results obtained from a $2 \times 2 \times 2$ cubic supercell, containing 63 atoms. Defect level $2p$ has a spin splitting of 0.4 eV. Results in column "GW bulk" were obtained by Hybertsen and Louie[2] for bulk LiCl.

	LDA	GW_f+BSE	GW bulk[a]	Exp.[b,c]
L_v	0.43	−0.21	0.3	
Γ_v	0.64	0	0	0
$1s$	5.19	6.37		
$2p$	8.11	10.4–10.8		
Γ_c	6.96	9.35	9.1	9.4
L_c	7.06	9.63	9.7	
X_c	8.29	10.90–10.7		

[a]Reference 2.
[b]Reference 85.
[c]Reference 90.

mass models are not suitable due to the extremely large band gap, high effective masses, and small dielectric constant. Also, DFT suffers drawbacks due to the intrinsically underestimated band gap. Within the GW approximation, not only the band gap is correctly predicted, but defect states around the F center in LiCl can also be located.[86] Here, we go beyond and determine optical excitations and the dielectric function within BSE, and compare the results with the TDLDA prediction and with experiments.

Defect levels in LiCl are extremely localized, which simplifies considerably the numerical work. We simulate the defect by using a cubic supercell with 32 lithium and 32 chlorine atoms. The lattice parameter is taken from experiment. Starting from the ordered structure, one chlorine atom is removed and the Kohn-Sham equations are solved in real space with grid spacing 0.3 a.u. All atoms inside the periodic cell are allowed to move so as to minimize the total energy. Only atoms in the first lithium shell showed significant relaxation, with displacement of 0.05 a.u. and relaxation energy 30 meV. As a convergence test, the procedure was repeated in a much bigger cell, containing 216 atoms of each type (excluding the vacancy). Movement of atoms in the first shell was around 0.02 a.u. and relaxation energy less than 10 meV, thus showing the degree of localization of the defect. In the subsequent work, we used the 32Li+32Cl +vacancy cell. Since the presence of a vacancy breaks translational invariance, we reduced the Brillouin zone to the Γ point only, thus removing complications with Bloch functions and integrations over the Brillouin zone.[84]

Quasiparticle energies for the band edges and two defect levels are shown in Table V. This choice of supercell allows us to recognize easily the band edges at points Γ, L, and X by observing the symmetry properties of the calculated single-particle orbitals. Self-energy corrections in the neutral F center require the explicit inclusion of spin degrees of freedom: the $1s$ state is partially occupied with only one electron. Therefore, the self-energy operator was evaluated separately for the two possible spin configurations and the summation over occupied states in Eq. (23) performed over all occupied
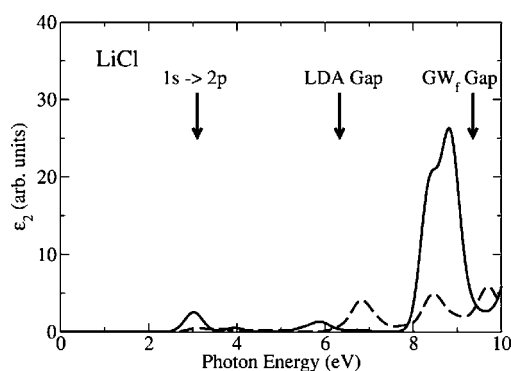

FIG. 9. Imaginary part of the macroscopic dielectric function, ϵ_2 for a F center embedded in LiCl. Solid and dashed lines correspond to GW+BSE and TDLDA calculations, respectively. The self-energy operator used in BSE is calculated within the GW_f approximation. The position of the $1s \rightarrow 2p$ transition line and electronic bands gaps within LDA and GW_f are shown with arrows. A Gaussian convolution with dispersion 0.2 eV was used to smear out the absorption lines.

states for each spin configuration. A similar procedure was used for the evaluation of the correlation and vertex parts of the self-energy. Although the self-energy operator is spin-dependent, most quasiparticle levels remain spin-degenerate, which is expected since there is no intrinsic source of spin polarization in the system. Table V shows that, within DFT-LDA, the $1s$ state is positioned inside the gap, but the $2p$ triplet state is located within the conduction band. Inclusion of self-energy corrections keeps the $2p$ triplet above the conduction band maximum (CBM). This phenomenon has been observed before.[86] Although mixed with extended states, the $2p$ triplet remains fairly localized within the vacancy. Indeed, 45% of its probability distribution is located within a distance of L_0 or less from the vacancy, where L_0 is the Li-Cl interatomic distance. For comparison, 74% of the $1s$ probability distribution is located within the same region.

Optical excitations in the system are calculated in both TDLDA and BSE frameworks. In both cases, spin polarization is included explicitly in the construction of the electron-hole kernel. Although not essential at the TDLDA level, the inclusion of spin polarization is important in the BSE because of the existence of the $1s$ partially occupied orbital. Figure 9 shows the imaginary part of the dielectric function for the cubic supercell containing 63 atoms. Although this crystal has an electronic band gap of 9.4 eV, the BSE spectrum is dominated by a wide double peak just below 9 eV. Being located below the band gap, this peak has the signature of excitonic effects.[8] The limited supercell size compromises resolution of the excitonic double peak and causes a redshift of 0.2 to 0.4 eV, although the overall features are consistent with calculations for a clean LiCl crystal. Below the excitonic peak, we can see one absorption line corresponding to the $1s \rightarrow 2p$ transition. In the real material, the strength of this line depends on temperature and density of defects, and so the calculated strength is somewhat arbitrary.

The absorption spectrum obtained within TDLDA is characteristic for the absence of the exciton peak. In fact, it has an onset at the DFT-LDA band gap, around 6.3 eV, followed

by a featureless rise towards higher energies. The three wide peaks in Fig. 9, located at 6.4, 8.3, and 9.7 eV are due to extremely limited resolution in the supercell. By including more atoms in the supercell, these peaks are expected to merge into a smooth function. The lack of excitonic effects in TDLDA has been reported in the literature.[7,18,21]

Surprisingly, TDLDA does predict a very accurate value for the $1s \rightarrow 2p$ transition energy: 3.10 eV, compared to 3.04 eV (BSE) and the measured value of 3.25 eV to 3.3 eV.[85,87–89] We believe this is related to the strong localization of both $1s$ and $2p$ orbitals. As discussed before, these orbitals are confined to within 1 or 2 atom sites from the vacancy. To some extent, the defect behaves as a confined electronic system, separated from the crystalline background. For transitions internal to this defect, such as the $1s \rightarrow 2p$, the LDA exchange-correlation kernel correctly describes electron-hole interactions. But transitions involving the conduction and/or valence bands are not so well described because the LDA kernel lacks the nonlocality present in electron-hole interactions involving extended orbitals. The BSE spectrum also shows a low feature at around 5.8 eV, which can be assigned to the $1s \rightarrow L$ line.[89]

IV. CONCLUSION

We discussed an implementation of Green's functions methods developed in the space of single-particle transitions. Contrary to alternative approaches, this procedure does not make use of Fourier analysis, and thus can be applied directly to confined systems, where it is particularly efficient. As an example, we are able to do a full GW+BSE calculation of the benzene molecule using a 1.7 GHz IBM Power4 machine in single-process mode in 280 min. This task requires no more than 600 MB of CPU memory and the only input required is the geometry of the molecule. Taking advantage of the extreme numerical efficiency of the current implementation, we are able to perform *ab initio* GW +BSE calculations of silicon clusters containing more than one hundred atoms.

Electronic screening is included within the TDLDA, and a corresponding vertex is included for consistency in the diagrammatic expansion. The added terms (TDLDA vertex +TDLDA screening) are found to be essential for accurate predictions of electron affinity and ionization potentials of benzene and naphthalene. This is in contrast with previous GW calculations which assume screening at the RPA level only but nevertheless provide accurate ionization potentials for small molecules.[8,9,17,19] The explanation for this apparent contradiction may be that the popularly used plasmon-pole models carry information about the exact many-body screening and therefore corrects deficiencies of the RPA.

Besides oligoacenes, the current implementation is used to investigate the absorption cross section of silicon clusters by solving the BSE. We conclude that, while the TDLDA and BSE differ markedly for small clusters, they agree in the broad features of the spectrum for large clusters. In particular, the dependence of excitation energy as function of cluster size is similar for both theories. The present results are consistent with QMC calculations for the minimum gap of sili-

con clusters. Excitation energies, ionization potentials, and electron affinities calculated within the present method are consistent with experimental data to within a fraction of eV, comparable to chemical accuracy.[91] In LiCl, we show how the existence of an F center affects the energy-resolved dielectric function. We also show that TDLDA predicts correctly the position of the $1s \rightarrow 2p$, despite producing a poor description of excitonic effects.

APPENDIX A: EVALUATION OF ENERGY INTEGRAL IN EQ. (22)

The derivation of Eqs. (23)–(25) from Eq. (22) follows from standard integration over poles.[3,37] For completeness, we present here the major steps. We start by defining separate exchange and correlation contributions in Eq. (22):

$$\langle j|\Sigma(E')|j'\rangle = \langle j|\Sigma_x|j'\rangle + \langle j|\Sigma_c(E')|j'\rangle \qquad (A1)$$

with

$$\langle j|\Sigma_x|j'\rangle = \int d\mathbf{r}_1 d\mathbf{r}_2 \varphi_j(\mathbf{r}_1) i \int \frac{dE}{2\pi} e^{-iE0^+}$$
$$\times G(\mathbf{r}_1,\mathbf{r}_2;E'-E)\varphi_{j'}(\mathbf{r}_2)V(\mathbf{r}_1,\mathbf{r}_2), \qquad (A2)$$

and

$$\langle j|\Sigma_c(E')|j'\rangle = \int d\mathbf{r}_1 d\mathbf{r}_2 \varphi_j(\mathbf{r}_1) i \int \frac{dE}{2\pi} e^{-iE0^+}$$
$$\times G(\mathbf{r}_1,\mathbf{r}_2;E'-E)\varphi_{j'}(\mathbf{r}_2)$$
$$\times \left[\int d\mathbf{r}_3 d\mathbf{r}_4 V(\mathbf{r}_1,\mathbf{r}_3)\Pi_0(\mathbf{r}_3,\mathbf{r}_4;E)V(\mathbf{r}_4,\mathbf{r}_2) \right].$$
$$(A3)$$

We assume a quasiparticle approximation for the one-electron Green's function,

$$G(\mathbf{r}_1,\mathbf{r}_2;E) = \sum_n \frac{\varphi_n(\mathbf{r}_1)\varphi_n(\mathbf{r}_2)}{E - \varepsilon_n + i\eta_n 0^+}. \qquad (A4)$$

In the exchange term, Eq. (A2), the only poles present are the ones originated from the Green's function. Therefore, the energy integration is easily replaced with a summation over occupied states only, resulting in Eq. (23). For the correlation term, Eq. (A3), we assume a polarizability operator given by Eq. (2). Now, both G and Π_0 contribute with poles below the real energy axis. Collecting them, one arrives at Eq. (24).

APPENDIX B: STATIC REMAINDER IN SELF-ENERGY

In most cases, the summation over n in Eqs. (24) and (30) has slow convergence. This behavior is not unique to the present implementation and it has also been observed in self-energy calculations when the dielectric matrix is explicitly computed in reciprocal space.[2,4,92] In that case, converged self-energies were found to require in excess of 100 unoccupied bands in the single-particle Green's function. The convergence rate can be accelerated by truncating this summation at some point and evaluating the remainder within the COHSEX (Coulomb hole + screened exchange) approximation.[4] The COHSEX approximation is essentially a static limit of Eq. (22). Assuming that screening is instantaneous, the polarizability Π_0 and the potential W_0 become proportional to a δ-function in time and constant in energy. The integral over energy in Eq. (22) can then be replaced by a sum over poles of the single-particle Green's function. In our implementation, one can recover the COHSEX approximation by imposing $\omega_s \gg |E - \varepsilon_n|$ in Eq. (24):

$$\langle j|\Sigma_c(E)|j'\rangle|_{COHSEX} = 4 \sum_{n}^{occ} \sum_{s} \frac{V_{nj}^s V_{nj'}^s}{\omega_s} - 2\sum_{n}\sum_{s} \frac{V_{nj}^s V_{nj'}^s}{\omega_s}. \quad \text{(B1)}$$

The last summation on n is done over all Kohn-Sham eigenstates. We evaluate it exactly by using a completeness relation. Using Eqs. (2), (3), (6), and (25), we obtain:

$$\langle j|\Sigma_c(E)|j'\rangle|_{COHSEX} = 4 \sum_{n}^{occ} \sum_{s} \frac{V_{nj}^s V_{nj'}^s}{\omega_s}$$
$$+ \frac{1}{2} \int d\mathbf{r}\, \varphi_j(\mathbf{r}) \widetilde{W}(\mathbf{r}) \varphi_{j'}(\mathbf{r}), \quad \text{(B2)}$$

where

$$\widetilde{W}(\mathbf{r}) = \frac{1}{2} \int d\mathbf{r}' \int d\mathbf{r}'' V(\mathbf{r},\mathbf{r}') \Pi_0(\mathbf{r}',\mathbf{r}'';E=0) V(\mathbf{r}'',\mathbf{r}).$$

Equations (B1) and (B2) can be used to determine the effect of truncating the sum over n at a value $N \gg n_{occ}$. The remainder then is

$$R_{jj'}^c(N) = \frac{1}{2} \int d\mathbf{r}\, \varphi_j(\mathbf{r}) \varphi_{j'}(\mathbf{r}) \int d\mathbf{r}'$$
$$\times \int d\mathbf{r}'' V(\mathbf{r},\mathbf{r}') \Pi_0(\mathbf{r}',\mathbf{r}'';0) V(\mathbf{r}'',\mathbf{r})$$
$$+ 2\sum_{n=1}^{N}\sum_{s} \frac{V_{nj}^s V_{nj'}^s}{\omega_s}. \quad \text{(B3)}$$

Although the COHSEX approximation has a level of accuracy lower than the full GW method, the convergence behavior is similar in both approximations if N is chosen sufficiently high. Equation (24) can then be replaced with

$$\langle j|\Sigma_c(E)|j'\rangle = R_{jj'}^c(N) + 2\sum_{n=1}^{N}\sum_{s} \frac{V_{nj}^s V_{nj'}^s}{E - \varepsilon_n - \omega_s \eta_n}. \quad \text{(B4)}$$

Along similar lines, the vertex term, Eq. (30) is rewritten as

$$\langle j|\Sigma_f(E)|j'\rangle = \sum_{n=1}^{N}\sum_{s} \frac{V_{nj}^s F_{nj'}^s + F_{nj}^s V_{nj'}^s}{E - \varepsilon_n - \omega_s \eta_n} + R_{jj'}^f(N), \quad \text{(B5)}$$

with

$$R_{jj'}^f(N) = \sum_{n=1}^{N}\sum_{s} \frac{V_{nj}^s F_{nj'}^s + F_{nj}^s V_{nj'}^s}{\omega_s}$$
$$+ \frac{1}{4} \int d\mathbf{r}\, \varphi_j(\mathbf{r}) \varphi_{j'}(\mathbf{r}) \int d\mathbf{r}' [V(\mathbf{r},\mathbf{r}')\Pi_f(\mathbf{r}',\mathbf{r};0)f(\mathbf{r})$$
$$+ f(\mathbf{r})\Pi_f(\mathbf{r},\mathbf{r}';0)V(\mathbf{r}',\mathbf{r})]. \quad \text{(B6)}$$

As an example, we have computed self-energy corrections in benzene including and not including the static remainder. With a static remainder, the first ionization energy decreases by 20 meV when N increases from 256 to 512, resulting in an ionization potential of 9.30 eV for the larger value of N. Without static remainder, this ionization energy increases by 133 meV between the same choices of N, and its value for $N=512$ is 8.27 eV, which is still far from convergence by as much as 1 eV.

In molecules and clusters, high-energy virtual states are expected to be very delocalized, and therefore sensitive to the choice of boundary conditions. In spite of that, the use of confined-system boundary conditions (where all wave functions are required to vanish outside some spherical enclosure) is still justified. The reason is that, as shown in Eq. (24), only the overlap between high-energy and low-energy states is relevant for self-energy calculations. The detailed features of high-energy states in the vacuum region, away from the atoms, are not very important. In addition, the contribution of virtual states in the summations over n decreases as one goes to higher and higher states. Nevertheless, the size of the confining region should always be tested against convergence, so that the shape of virtual states in the vicinity of atoms is correctly described.

---

[1] R. M. Martin, *Electronic Structure, Basic Theory and Practical Methods* (Cambridge University Press, Cambridge, 2004); R. G. Parr and W. Yang, *Density-functional theory of atoms and molecules* (Oxford University Press, Oxford, England, 1989); M. C. Payne, M. P. Teter, D. C. Allan, T. A. Arias, and J. D. Joannopo-ulos, Rev. Mod. Phys. **64**, 1045 (1992).

[2] M. S. Hybertsen and S. G. Louie, Phys. Rev. B **34**, 5390 (1986).

[3] L. Hedin and S. Lundqvist, *Solid State Physics*, edited by F. Seitz, D. Turnbull, and H. Ehrenreich (Academic, New York, 1969), Vol. 23, p. 1.

[4] W. G. Aulbur, L. Jönsson, and J. W. Wilkins, *Solid State Physics*, edited by F. Seitz, D. Turnbull, and H. Ehrenreich (Academic, New York, 2000), Vol. 54, p. 1.

[5] A. Görling, H. H. Heinze, S. Ph. Ruzankin, M. Staufer, and N. Rösch, J. Chem. Phys. **110**, 2785 (1999).

[6] P. Rinke, A. Qteish, J. Neugebauer, C. Freysoldt, and M. Scheffler, New J. Phys. **7**, 126 (2005); M. Städele, M. Moukara, J. A. Majewski, P. Vogl, and A. Görling, Phys. Rev. B **59**, 10031 (1999).

[7] G. Onida, L. Reining, and A. Rubio, Rev. Mod. Phys. **74**, 601 (2002).

[8] M. Rohlfing and S. G. Louie, Phys. Rev. B **62**, 4927 (2000).

[9] M. Rohlfing, Int. J. Quantum Chem. **80**, 807 (2000).

[10] S. Albrecht, L. Reining, R. Del Sole, and G. Onida, Phys. Rev. Lett. **80**, 4510 (1998); C. D. Spataru, S. Ismail-Beigi, L. X. Benedict, and S. G. Louie, *ibid.* **92**, 077402 (2004); M. Rohlfing and S. G. Louie, *ibid.* **82**, 1959 (1999); E. Chang, G. Bussi, A. Ruini, and E. Molinari, *ibid.* **92**, 196401 (2004); J.-W. van der Horst, P. A. Bobbert, M. A. J. Michels, and H. Bassler, J. Chem. Phys. **114**, 6950 (2001); P. Puschnig and C. Ambrosch-Draxl, Phys. Rev. Lett. **89**, 056405 (2002).

[11] M. L. Tiago, J. E. Northrup, and S. G. Louie, Phys. Rev. B **67**, 115212 (2003).

[12] J. C. Grossman, M. Rohlfing, L. Mitas, S. G. Louie, and M. L. Cohen, Phys. Rev. Lett. **86**, 472 (2001).

[13] H.-J. Eisler, V. C. Sundar, M. G. Bawendi, M. Walsh, H. I. Smith, and V. Klimov, Appl. Phys. Lett. **80**, 4614 (2002); K. Ichimura, S.-K. Oh, and M. Nakagawa, Science **288**, 1624 (2000).

[14] V. N. Soloviev, A. Eichhöfer, D. Fenske, and U. Banin, J. Am. Chem. Soc. **123**, 2354 (2001); A. P. Alivisatos, Science **271**, 933 (1996).

[15] T. A. Niehaus, M. Rohlfing, F. Della Sala, A. Di Carlo, and Th. Frauenheim, Phys. Rev. A **71**, 022508 (2005).

[16] P. H. Hahn, W. G. Schmidt, and F. Bechstedt, Phys. Rev. B **72**, 245425 (2005).

[17] S. Ismail-Beigi and S. G. Louie, Phys. Rev. Lett. **90**, 076401 (2003).

[18] L. X. Benedict, A. Puzder, A. J. Williamson, J. C. Grossman, G. Galli, J. E. Klepeis, J.-Y. Raty, and O. Pankratov, Phys. Rev. B **68**, 085310 (2003).

[19] S. Ishii, K. Ohno, Y. Kawazoe, and S. G. Louie, Phys. Rev. B **63**, 155104 (2001); S. Ishii, K. Ohno, Y. Kawazoe, and S. G. Louie, *ibid.* **65**, 245109 (2002).

[20] I. Vasiliev, S. Öğüt, and J. R. Chelikowsky, Phys. Rev. B **65**, 115416 (2002).

[21] L. Reining, V. Olevano, A. Rubio, and G. Onida, Phys. Rev. Lett. **88**, 066404 (2002).

[22] R. Del Sole, O. Pulci, V. Olevano, and A. Marini, Phys. Status Solidi B **242**, 2729 (2005); U. von Barth, N. E. Dahlen, R. van Leeuwen, and G. Stefanucci, Phys. Rev. B **72**, 235109 (2005).

[23] A. Marini, R. Del Sole, and A. Rubio, Phys. Rev. Lett. **91**, 256402 (2003); F. Sottile, V. Olevano, and L. Reining, *ibid.* **91**, 056402 (2003); S. Botti, A. Fourreau, F. Nguyen, Y. O. Renault, F. Sottile, and L. Reining, Phys. Rev. B **72**, 125203 (2005); S. Botti, F. Sottile, N. Vast, V. Olevano, L. Reining, H. C. Weissker, A. Rubio, G. Onida, R. Del Sole, and R. W. Godby, *ibid.* **69**, 155112 (2004); G. Adragna, R. Del Sole, and A. Marini, *ibid.* **68**, 165108 (2003).

[24] F. Bruneval, F. Sottile, V. Olevano, R. Del Sole, and L. Reining, Phys. Rev. Lett. **94**, 186402 (2005).

[25] F. Sottile, F. Bruneval, A. G. Marinopoulos, L. K. Dash, S. Botti, V. Olevano, N. Vast, A. Rubio, and L. Reining, Int. J. Quantum Chem. **102**, 684 (2005).

[26] M. L. Tiago and J. R. Chelikowsky, Solid State Commun. **136**, 333 (2005).

[27] E. K. U. Gross and W. Kohn, Phys. Rev. Lett. **55**, 2850 (1985); Adv. Quantum Chem. **21**, 255 (1990).

[28] M. E. Casida, in *Recent Advances in Density-Functional Methods*, edited by D. P. Chong (World Scientific, Singapore, 1995), Part I, p. 155.

[29] M. E. Casida, C. Jamorski, K. C. Casida, and D. R. Salahub, J. Chem. Phys. **108**, 4439 (1998).

[30] C. Jamorski, M. E. Casida, and D. R. Salahub, J. Chem. Phys. **104**, 5134 (1996).

[31] G. Strinati, Riv. Nuovo Cimento **11**, 1 (1988).

[32] W. Kohn and L. J. Sham, Phys. Rev. **140**, A1133 (1965).

[33] S. L. Adler, Phys. Rev. **126**, 413 (1962); N. Wiser, *ibid.* **129**, 62 (1963).

[34] S. Öğüt, R. Burdick, Y. Saad, and J. R. Chelikowsky, Phys. Rev. Lett. **90**, 127401 (2003).

[35] R. W. Godby, M. Schlüter, and L. J. Sham, Phys. Rev. B **37**, 10159 (1988).

[36] E. L. Shirley and R. M. Martin, Phys. Rev. B **47**, 15404 (1993); **47**, 15413 (1993).

[37] L. Hedin, Int. J. Quantum Chem. **56**, 445 (1995).

[38] R. Del Sole, L. Reining, and R. W. Godby, Phys. Rev. B **49**, 8024 (1994).

[39] A. Fleszar and W. Hanke, Phys. Rev. B **71**, 045207 (2005); S. V. Faleev, M. van Schilfgaarde, and T. Kotani, Phys. Rev. Lett. **93**, 126406 (2004); W. Ku and A. G. Eguiluz, *ibid.* **89**, 126401 (2002); W. Ku and A. G. Eguiluz, *ibid.* **93**, 249702 (2004); K. Delaney, P. García-González, A. Rubio, P. Rinke, and R. W. Godby, Phys. Rev. Lett. **93**, 249701 (2004); M. L. Tiago, S. Ismail-Beigi, and S. G. Louie, Phys. Rev. B **69**, 125212 (2004); R. T. M. Ummels, P. A. Bobbert, and W. van Haeringen, *ibid.* **57**, 11962 (1998).

[40] D. F. DuBois, Ann. Phys. (Paris) **7**, 174 (1959); **8**, 24 (1959).

[41] B. Holm and U. von Barth, Phys. Rev. B **57**, 2108 (1998); U. von Barth and B. Holm, *ibid.* **54**, 8411 (1996); *ibid.* **55**, 10120(E) (1997).

[42] F. Furche, J. Chem. Phys. **114**, 5982 (2001); B. Walker, A. M. Saitta, R. Gebauer, and S. Baroni, Phys. Rev. Lett. **96**, 113001 (2006).

[43] J. P. Perdew and A. Zunger, Phys. Rev. B **23**, 5048 (1981); D. M. Ceperley and B. J. Alder, Phys. Rev. Lett. **45**, 566 (1980).

[44] N. Troullier and J. L. Martins, Phys. Rev. B **43**, 1993 (1991).

[45] J. R. Chelikowsky, N. Troullier, and Y. Saad, Phys. Rev. Lett. **72**, 1240 (1994); J. R. Chelikowsky, N. Troullier, K. Wu, and Y. Saad, Phys. Rev. B **50**, 11355 (1994).

[46] *NIST Chemistry Webbook, NIST Standard Reference Database*, edited by P. J. Linstrom and W. G. Mallard (National Institute of Standards and Technology, Gaithersburg, MD, 2001), Number 69 (http://webbook.nist.gov).

[47] G. F. Bertsch, A. Schnell, and K. Yabana, J. Chem. Phys. **115**, 4051 (2001).

[48] S. P. Park, S. S. Kim, J. H. Kim, C. N. Whang, and S. Im, Appl. Phys. Lett. **80**, 2872 (2002).

[49] J. B. Krieger, Y. Li, and G. J. Iafrate, Phys. Rev. A **45**, 101 (1992).

[50] J. F. Janak, Phys. Rev. B **18**, 7165 (1978).

[51] C.-G. Zhan, J. A. Nichols, and D. A. Dixon, J. Phys. Chem. A **107**, 4184 (2003).

[52] F. Della Sala and A. Görling, J. Chem. Phys. **115**, 5718 (2001).

[53] A. Görling, Phys. Rev. Lett. **83**, 5459 (1999).

[54] N. O. Lipari, C. B. Duke, and L. Prietronero, J. Chem. Phys. **65**, 1165 (1976).

[55] M. S. Deleuze, L. Claes, E. S. Kryachko, and J.-P. François, J. Chem. Phys. **119**, 3106 (2003).

[56] S. Hirata, C.-G. Zhan, E. Aprà, T. L. Windus, and D. A. Dixon, J. Phys. Chem. A **107**, 10154 (2003).

[57] J. C. Rienstra-Kiracofe, C. J. Barden, S. T. Brown, and H. F. Schaefer III, J. Phys. Chem. A **105**, 524 (2001).

[58] P. D. Burrow, J. A. Michejda, and K. D. Jordan, J. Chem. Phys. **86**, 9 (1987).

[59] I. Vasiliev and R. M. Martin, Phys. Rev. A **69**, 052508 (2004).

[60] G. Herzberg, *Molecular Spectra and Molecular Structure, Electronic Spectra and Electronic Structure of Polyatomic Molecules* (Van Nostrand, New York, 1966), Vol. III.

[61] E. E. Koch and A. Otto, Chem. Phys. Lett. **12**, 476 (1976).

[62] J. Lorentzon, P. Malmquist, M. Fülscher, and B. O. Roos, Theor. Chim. Acta **91**, 91 (1995).

[63] H. H. Heinze, A. Görling, and N. Rösch, J. Chem. Phys. **113**, 2088 (2000).

[64] J. P. Doering, J. Chem. Phys. **51**, 2866 (1969).

[65] M. Rubio, M. Merchán, E. Orti, and B. O. Roos, Chem. Phys. **179**, 395 (1993).

[66] G. A. George and G. C. Morris, J. Mol. Spectrosc. **26**, 67 (1968).

[67] M. J. S. Dewar and S. D. Worley, J. Chem. Phys. **50**, 654 (1969).

[68] B. C. Lin, C. P. Cheng, and Z. P. M. Lao, J. Phys. Chem. A **107**, 5241 (2003).

[69] T. Heinis, S. Chowdhury, and P. Kebarle, Org. Mass Spectrom. **28**, 358 (1993).

[70] A. Zlatkis, C. K. Lee, and W. E. Wentworth, Anal. Chem. **55**, 1596 (1983).

[71] U. Itoh, Y. Toyoshima, and H. Onuki, J. Chem. Phys. **85**, 4867 (1986).

[72] L. Mitas, J. Therrien, R. Twesten, G. Belomoin, and M. H. Nayfeh, Appl. Phys. Lett. **78**, 1918 (2001).

[73] Y.-H. Kim and A. Görling, Phys. Rev. Lett. **89**, 096402 (2002).

[74] L. E. Brus, J. Chem. Phys. **79**, 5566 (1983); **80**, 4403 (1984).

[75] L. A. Cole and J. P. Perdew, Phys. Rev. A **25**, 1265 (1982).

[76] M. Rohlfing and S. G. Louie, Phys. Rev. Lett. **80**, 3320 (1998).

[77] V. Olevano and L. Reining, Phys. Rev. Lett. **86**, 5962 (2001).

[78] M. Born and E. Wolf, *Principles of Optics: Electromagnetic Theory of Propagation, Interference and Diffraction of Light*, 7th ed. (Cambridge University Press, Cambridge, 1999), Sect. 14.5; J. C. Maxwell-Garnett, Philos. Trans. R. Soc. London

203A, 385 (1904).

[79] A. Tsolakidis and R. M. Martin, Phys. Rev. B **71**, 125319 (2005).

[80] X. Zhao, C. M. Wei, L. Yang, and M. Y. Chou, Phys. Rev. Lett. **92**, 236805 (2004); F. Bruneval, S. Botti, and L. Reining, *ibid.* **94**, 219701 (2005); X. Zhao, C. M. Wei, L. Yang, and M. Y. Chou, *ibid.* **94**, 219702 (2005).

[81] W. Hanke, Adv. Phys. **27**, 287 (1978).

[82] B. Delley and E. F. Steigmeier, Phys. Rev. B **47**, 1397 (1993).

[83] A. J. Williamson, J. C. Grossman, R. Q. Hood, A. Puzder, and G. Galli, Phys. Rev. Lett. **89**, 196803 (2002).

[84] M. M. G. Alemany, M. Jain, L. Kronik, and J. R. Chelikowsky, Phys. Rev. B **69**, 075101 (2004).

[85] G. Baldini and B. Bosacchi, Phys. Status Solidi **38**, 325 (1970).

[86] M. P. Surh, H. Chacham, and S. G. Louie, Phys. Rev. B **51**, 7464 (1995).

[87] C. J. Buchenauer and D. B. Fitchen, Phys. Rev. **167**, 846 (1968).

[88] K. Takiyama, J. Phys. Soc. Jpn. **44**, 1627 (1978).

[89] C. C. Klick, Phys. Rev. **137**, A1814 (1965).

[90] F. C. Brown, Ch. Gähwiller, H. Fujita, A. B. Kunz, W. Scheifley, and N. Carrera, Phys. Rev. B **2**, 2126 (1970).

[91] L. A. Curtiss, P. C. Redfern, K. Raghavachari, and J. A. Pople, J. Chem. Phys. **109**, 42 (2003); L. A. Curtiss, K. Raghavachari, P. C. Redfern, V. Rassolov, and J. A. Pople, *ibid.* **109**, 7764 (2003).

[92] L. Reining, G. Onida, and R. W. Godby, Phys. Rev. B **56**, R4301 (1997).

[93] As written, Eq. (2) corresponds to a time-ordered function, but it differs from the causal (measurable) response function only for negative values of energy.

[94] Confirming earlier work,[8] we have observed that the Tamm-Dancoff approximation (i.e., neglecting mixing between absorption and emission contributions) is acceptable when calculating excitation energies in the GW+BSE framework. This contrasts with the scenario in TDDFT, where mixing is usually important,[7,28,42] due to the specific properties of the TDDFT kernels. The impact of the Tamm-Dancoff approximation in the energy loss spectrum of silicon has been analyzed by Olevano and Reining.[77]

[95] The value of 7.4 eV reported in Ref. 20 for the peak position has been recently revised to 7.1 eV in Ref. 59.

[96] The inaccurate optical gap reflects the gap underestimation inherent to DFT, and it can be corrected by an *ad hoc* scissors operator. The lack of excitonic effects should be attributed to the specific functional employed in TDLDA, since other functionals were shown to correctly predict the enhancement of the E_1 peak relative to E_2 (Refs. 21 and 73).